Journal of Materials Chemistry A

ROYAL SOCIETY OF CHEMISTRY

PERSPECTIVE

View Article Online
View Journal | View Issue

Cite this: J. Mater. Chem. A, 2021, 9, 18793

Emerging elemental two-dimensional materials for energy applications

Zongxiao Wu,† Junlei Qi,† Wenbin Wang, Zhiyuan Zeng and Qiyuan He *

Elemental two-dimensional (2D) materials possess distinct properties and superior performances across a multitude of fundamental and practical research fields. Although a tremendous number of earlier studies focus on graphene and its derivatives, other emerging elemental 2D materials, such as borophene, silicene, black phosphorene, antimonene, tellurene, bismuthene and arsenene, are attracting increasing research interest in electronics and optoelectronics, as well as various energy storage and conversion applications, owing to their unique structural, electrochemical and electronic properties. In particular, emerging elemental 2D materials often possess large surface areas, high theoretical capacity, structural anisotropicity, high carrier mobility and tunable bandgaps, making them promising candidates in many energy storage and conversion technologies. Recently, we have witnessed remarkable progress in the preparation, characterization, and application of many emerging elemental 2D materials. However, the challenging yet vastly different synthetic strategies and resulting physicochemical properties, along with complex theoretical and experimental results, make it difficult to navigate through their applications in specific research fields. In this perspective, we summarize the progress of emerging elemental 2D materials in terms of their preparation methods, properties and figures of merit in energy storage and catalytic applications. Furthermore, we present our insight into the challenges and opportunities, which would hopefully shed light on the great potential of this ever-expanding field.

Received 1st May 2021
Accepted 25th June 2021

DOI: 10.1039/d1ta03676a

rsc.li/materials-a

Department of Materials Science and Engineering, City University of Hong Kong, Hong Kong SAR, China. E-mail: qiyuanhe@cityu.edu.hk

† These authors contributed equally to this work.

Dr Qiyuan He is currently an Assistant Professor in the Department of Materials Science & Engineering at the City University of Hong Kong. He obtained his PhD Degree from Nanyang Technological University in Singapore in 2013. He then joined the University of California, Los Angeles as a Postdoctoral Fellow before returning to Nanyang Technological University as a Research Fellow in 2016. Dr He's research scope is highly interdisciplinary, focusing on the fundamentals of semiconductor interfaces and their applications in nanoelectronics, iontronics, chemical/biological sensors, catalysis, and on-chip electrochemistry, and of course, Star Wars.

1. Introduction

The discovery of graphene has sparked tremendous interest in two-dimensional (2D) materials in both fundamental and practical research for well over a decade, owing to their many unique physical and chemical properties.[1,2] In particular, the atomic-thin morphology, large surface area and layered structure make them ideal candidates for energy devices. Looking beyond graphene, researchers have also explored a variety of 2D materials, such as hexagonal boron nitride (h-BN)[3] and transition metal dichalcogenides (TMDs).[4] Among the enormous 2D materials family, elemental 2D materials are one unique type of elemental material with 2D layered or sheet-like structures, often referred to as Xenes, demonstrating promising prospects in electronic and energy fields.[5–7] Compared with TMDs, which usually exhibit indirect bandgaps, many elemental 2D materials possess superior mobility (tellurene, black arsenene, *etc.*) and direct band gaps (BP, black arsenene, *etc.*). While reviews of elemental 2D materials in electronics could be found previously,[8–11] in this perspective, we will elaborate on the recent advances of elemental 2D materials in the fields of energy storage and catalysis.

Until now, over a dozen elemental 2D materials have been experimentally realized, with more still in theoretical predictions.[12–14] An overview of all the theoretically and experimentally explored elemental 2D materials is shown in Table 1. Due to the

Table 1 Overview of elemental 2D materials explored by experimental and theoretical methods. The shaded elements are yet to be explored by any method. Aluminene and indiene are currently only theoretically predicted. *Th.* represents theoretical exploration. Generally, several allotropes of one elemental 2D material exist in experiments or theoretical predictions. The experimental realization and theoretical prediction can be found in ref. 15, 17 and 37–51

13	14	15	16	17
5 **B**	6 **C**	7 **N**	8 **O**	9 **F**
13 **Al** *(Th.)*	14 **Si**	15 **P**	16 **S**	17 **Cl**
31 **Ga**	32 **Ge**	33 **As**	34 **Se**	35 **Br**
49 **In** *(Th.)*	50 **Sn**	51 **Sb**	52 **Te**	53 **I**
81 **Ti**	82 **Pb**	83 **Bi**	83 **Po**	85 **At**

vast different synthetic strategies and properties,[5] we resolve to use the most straightforward categorization according to element groups. For group 13 elements, the monolayer structures of two elements, boron and gallium, have been successfully synthesized and termed borophene and gallenene,[15–30] respectively. Due to the carbon-neighbor position of boron in the periodic table of elements, borophene is expected to possess some properties similar to those of graphene,[16] such as high capacity, and electronic and ionic conductivity, indicating prospects for use in metal ion batteries as an anode material. Similarly, with atomic structures analogous to graphene, silicene (2D silicon), germanene (2D germanium), stanene (2D tin) and plumbene (2D lead) in group 14 have also been experimentally explored. Tunable bandgaps with various surface engineering strategies are their most attractive properties, offering a fascinating prospect of discrete engineering applications.[31]

In group 15, black phosphorene (denoted as BP) remains the most explored elemental 2D material besides graphene. Previously, 2D black phosphorus was commonly denoted as phosphorene or simply black phosphorus. However, novel allotropes, such as violet phosphorene[32] and blue phosphorene,[33] have recently been synthesized. Thereby, we use the term BP to represent black phosphorene. Few-layer BP exhibits significantly higher carrier mobility and larger theoretical capacity for metal-ion batteries than other 2D materials.[34] Additionally, its tunable bandgap and abundant active sites are favorable for catalytic applications.[35] However, the inferior stability of BP limits its practical application, which remains an important barrier to overcome. Furthermore, other elemental 2D materials in groups 15 and 16 with analogous lattice structures to BP, *i.e.*, arsenene (2D As), antimonene (2D Sb), bismuthene (2D Bi), and tellurene (2D Te), exhibiting tunable band gaps, high carrier mobility, high theoretical capacity, and more importantly, excellent environmental stability, are being actively pursued theoretically and experimentally.[36] They provide a wide range of potential candidates for high-performance electrode materials with good stability in energy storage and conversion fields.

In this perspective, we highlight the ever-expanding family of elemental 2D materials and their intriguing applications in energy storage, including batteries and supercapacitors, and energy conversion, including electrocatalysis, photocatalysis and solar cells. Firstly, we provide an overview of the basic properties of emerging elemental 2D materials, followed by a comprehensive summary of their synthetic methods. Next, their figures of merit in specific fields of energy storage and conversion are discussed. Finally, we share our perspective on the challenges and opportunities in this developing research field and hope to shed some light on the fundamental exploration and future application.

2. Structures and properties

2.1 Elemental 2D materials of group 13

Both borophene (2D boron) and gallenene (2D gallium) show high anisotropy due to the different arrangements of atoms along two different lattice directions. Many different phases of borophene, such as 2-*Pmmn*, β_{12}, χ_3, and honeycomb (Fig. 1a–d), have been synthesized and relatively comprehensively studied.[15,20,26] For example, the 2-*Pmmn* phase holds a bulked structure with slight corrugation along the ***a*** direction (zigzag direction). But along the ***b*** direction (armchair direction), the corrugations of this structure are removed. 2-*Pmmn* borophene is predicted to have great anisotropy in the electronic band structure, exhibiting metallic properties along the armchair direction while possessing a large bandgap in the zigzag direction.[15] The excellent electron and ion transport along the armchair direction and the high capacity make borophene an attractive material in ion batteries. In contrast to the 2-*Pmmn* phase, other obtained structures (β_{12}, χ_3, and the honeycomb) are all planar, which can be attributed to the weak interaction with the underlying substrate. As shown in Fig. 1b and c, the sheet structures of β_{12} and χ_3 are similar, with the main difference being the hexagonal boron array for the β_{12} phase and the narrow zigzag boron array for the χ_3 phase.[20] In particular, honeycomb borophene shows a V-shape dI/dV curve *via* scanning tunneling spectroscopy (STS) near the Fermi energy, suggesting the Dirac band structures similar to graphene.[26] Additionally, the χ_6 and γ-B_{28} phases of borophene have been successfully synthesized with study on their properties still in progress.[28]

Two stable 2D anisotropies of gallenene have been recently synthesized, which, again, show both buckled and planar configurations (as shown in Fig. 1e and f), respectively.[17,52] Due

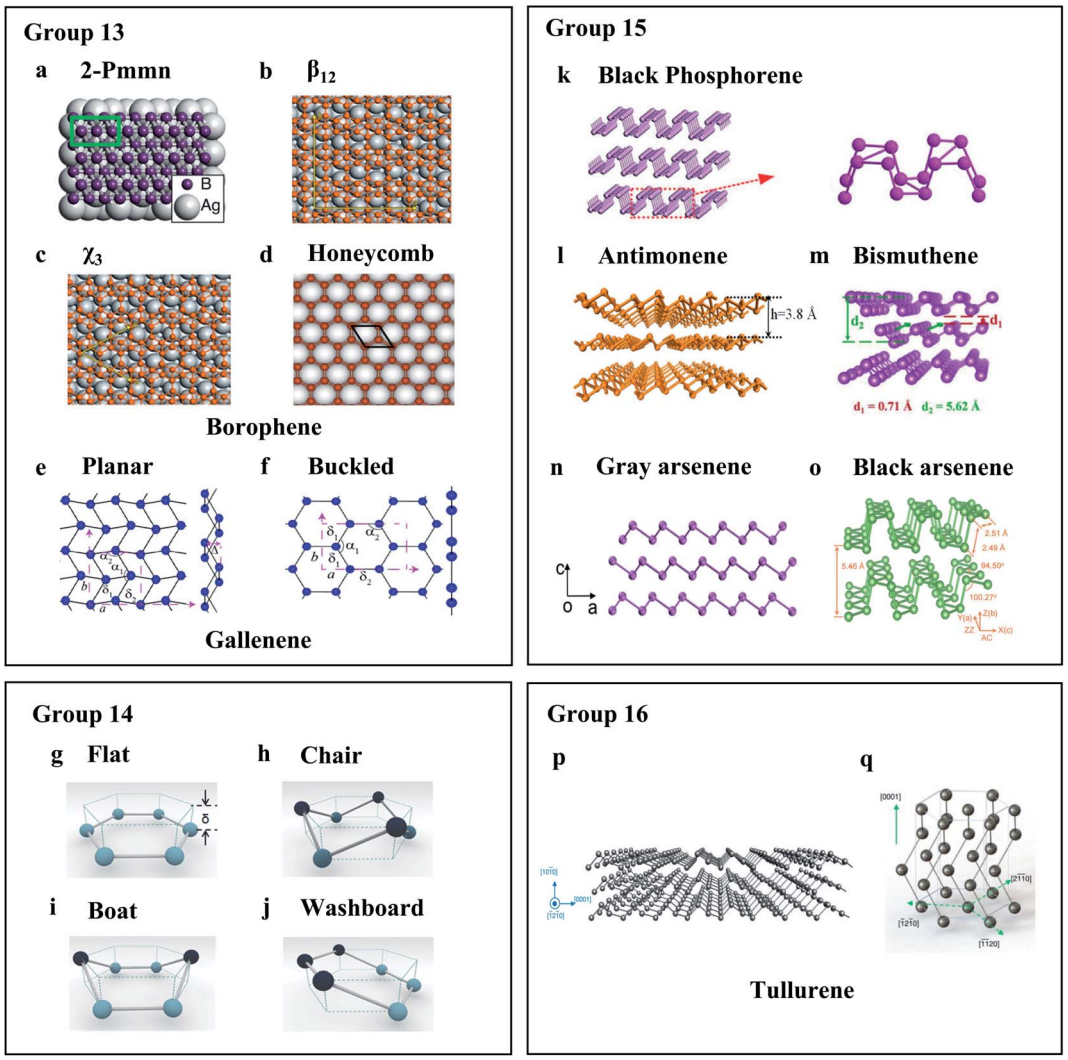

Fig. 1 Crystal structures of elemental 2D materials. (a) 2-*Pmmn*, (b) β_{12}, (c) χ_3, and (d) honeycomb borophene.[14,25,36] (a) Reproduced with permission,[14] American Association for the Advancement of Science (AAAS). (b) and (c) Reproduced with permission,[25] Springer Nature. (d) Reproduced with permission,[36] Elsevier. (e) Planar and (f) buckled gallenene. Reproduced with permission,[38] AAAS. (g)–(j) Theoretical buckled hexagonal structures of group 14 elemental materials. Reproduced with permission,[40] Wiley-VCH. (g) Flat; (h) chair; (i) boat and (j) washboard. (k) Black phosphorene. Reproduced with permission,[53] Wiley-VCH. (l) Antimonene. Reproduced with permission,[62] American Chemical Society. (m) Bismuthene. Reproduced with permission,[68] Wiley-VCH. (n) Grey arsenene. Reproduced with permission,[76] American Chemical Society. (o) Black arsenene. Reproduced with permission,[78] Wiley-VCH. (p) and (q) Tellurene from the [1$\bar{2}$10] direction (p) and front view (q). Reproduced with permission,[81] Springer Nature.

to the finite density of states at the Fermi energy, both allotropes of gallenene show metallic characteristics, however, with different band structures. The bands of buckled configuration are highly dispersive with a large bandwidth, suggesting lighter charge carriers and higher mobilities.

2.2 Elemental 2D materials of group 14

In contrast to graphene, most elemental 2D materials in group 14 (silicene,[37] germanene,[38] stanene,[39] and plumbene[40]) show buckled honeycomb structures, resulting from the mixed hybridization of sp^3 and sp^2, except for the recent discovery of a planar stanene polymorph.[53,54] The buckling positions vary in the hexagonal buckled structures, termed chair, boat, and washboard, respectively.[55,56] Fig. 1g–j illustrates the flat and buckled hexagonal structure. The most stable structures for each element were also predicted, *i.e.*, triple-layer MoS_2 geometry for stanene, large honeycomb dumbbell arrangements for silicene and germanene, and high-buckled 2D phases for plumbene.[57,58] In addition, theoretical studies have predicted many "non-graphene" 2D carbons. Among them, the two most theoretically stable allotropes are phagraphene (consisting of 5-6-7 carbon rings) and penta-graphene (consisting entirely of pentagons).[41,42] Like 2D materials in group 13, buckled 2D materials in group 14 possess Dirac cone semimetal band structures.[59,60] For example, the band structures of various graphene allotropes are predicted to range from metallic[61,62] to wide bandgap semiconductors,[63,64] resulting from the different

degrees of sp^2 and sp^3 hybridization. For instance, penta-graphene may possess an intrinsic quasi-direct band gap of 3.25 eV,[42] which is close to that of ZnO and GaN, while phagraphene is metallic.[65]

2.3 Elemental 2D materials of group 15

The 2D forms of group 15 elements are similarly termed analogous to graphene, namely phosphorene (2D BP), arsenene (2D As), antimonene (2D Sb), and bismuthene (2D Bi), which exhibit different crystal orientations and band structures.

Black phosphorene (BP) possesses a side-centered layered orthorhombic lattice structure, the space group of which is classified as *Cmca*. For each P atom in the crystal lattice, there are three nearest neighbor P atoms. The puckered atom layers can be regarded as two parallel sub-layers within the plane (Fig. 1k).[43] And P atoms form two kinds of geometries (zigzag-like and armchair-like) along different directions, which lead to strong anisotropic properties. Also, the interlayer spacing of BP is about 0.53 nm,[66] larger than that of graphene (0.33 nm).[67] Such large interlayer spacing results from the puckered structure, as well as the AB Bernal stacking of two phosphorene layers in the unit cell.[68] Few-layer BP shows predominant p-type behavior, and is one among the few examples of p-type 2D materials along with WSe_2 and tellurene.[69] It maintains direct bandgaps, which can be tuned by its thickness from 0.3 eV (bulk) to 2 eV (monolayer).[70,71] Few-layer BP possesses high theoretical carrier mobility, *i.e.*, 10 000–26 000 $cm^2 V^{-1} s^{-1}$ for monolayer BP.[70] However, BP faces severe chemical degradation under ambient conditions. Tremendous efforts have been made to understand the exact mechanism of BP degradation from theoretical and experimental respects. With spectroscopic investigation, it was found that the oxidation process of BP is most likely directly related to the oxygen concentration and light density.[72] Additionally, Wang *et al.* found that O_2 spontaneously dissociates on the surface of few-layer BP under ambient conditions and consequently initializes the oxidation process.[73] In contrast to popular belief, H_2O would not directly interact with BP until it has been already oxidized. Most recently, researchers also successfully synthesized violet phosphorene[32] and blue phosphorene,[33] which are still at the primary stage of investigation.

For antimonene, β-phase antimonene is found to be the most thermodynamically stable phase. According to transmission electron microscope (TEM) characterization and calculations, β-antimonene exhibits a buckled hexagonal atomic structure with two atoms per unit cell and an interlayer distance of 3.73 Å (ref. 74) (Fig. 1l). Based on theoretical calculation results, β-antimony remains metallic until the thickness is reduced to two layers, and the monolayer antimonene exhibits a relatively large bandgap of 2.28 eV.[19] Experimentally, β-antimonene obtained by liquid-phase exfoliation shows thickness-dependent bandgaps between 0.8 eV (5–7 nm) and 1.44 eV (0.3–1 nm).[44] Moreover, unlike BP, β-antimonene shows good stability under ambient conditions. Verified by optical microscopy and Raman characterization, monolayer antimonene on a $PdTe_2$ substrate prepared *via* MBE showed no change in optical microscopy and Raman spectra after annealing at 380 K for 10 minutes before the oxidation begins.[75] Similarly, few-layer antimonene flakes prepared by chemical vapor deposition could remain stable for 10 minutes below 250 °C and show no change in Raman spectra for three months under ambient conditions at room temperature.[76]

Bismuthene is another relatively stable elemental 2D material of group 15. Analogous to antimonene, few-layer bismuthene also crystallizes with a buckled layered structure, which is the most thermodynamically stable phase among all its allotropies.[77] Monolayer bismuthene exhibits a 2D hexagonal lattice with a washboard structure (Fig. 1m).[45,78] The interlayer spacing of monolayer bismuthene is 3.9 Å,[45] which is smaller than that of BP, still generally favorable for ion intercalation in the electrochemical process. Although bulk bismuth remains metallic, few-layer bismuthene is predicted to be an n-type 2D semiconductor with direct bandgaps. Similar to BP, the bandgap of bismuthene is expected to be thickness dependent from 0 V (bulk) to 0.55 eV (monolayer).[78] Moreover, bismuthene may possess exceptionally high carrier mobility, ranging from 5.7×10^6 (bulk) to 20 000 $cm^2 V^{-1} s^{-1}$ (0.1–2 μm thin films), which is superior to that of few-layer BP.[79]

Arsenene has two thermodynamically stable phases, gray arsenene with a buckled lattice structure (Fig. 1n) and black arsenene with a puckered lattice structure (Fig. 1o). Both demonstrate better chemical stability than BP.[46,80] Gray arsenene has the *P*3*m*1 space group[81] and exhibits a lattice constant of 3.61 Å.[82] The atomic layers are stacked *via* ABC arrangement.[83,84] On the other hand, black arsenene is analogous to BP with a puckered structure.[85] It exhibits the *Pmna* space group[81] and an interlayer distance of 5.46 Å.[86] Both grey and black arsenene possess thickness-dependent indirect bandgaps. The bandgaps of monolayer grey and black arsenene are expected to be 1.63 and 0.83 eV, respectively,[81] which are yet to be experimentally confirmed. Besides, grey arsenene and black arsenene are expected to have moderate carrier mobilities of 527.40 $cm^2 V^{-1} s^{-1}$ (ref. 87) and 176.82 $cm^2 V^{-1} s^{-1}$,[88] respectively.

2.4 Elemental 2D materials of group 16

There are two phases of tellurene, α and β, with the α-phase being more thermodynamically stable. α-phase tellurene shows a trigonal crystal lattice similar to their bulk counterpart, in which Te atoms form individual helical chains and then spiral along axes parallel to the [0001] direction at the center and corners of the hexagonal elementary cell[89] (Fig. 1p and q). Each Te atom has two nearest atoms and is bonded *via* a covalent bond. Both the monolayer tellurene film MBE-grown on graphene layers[90] and free-standing few-layer tellurene nanosheets prepared through a wet-chemistry method[89] exhibit lattice constants consistent with the α-phase with trigonal configuration. On the other hand, the monolayer tellurene film MBE-grown on highly oriented pyrolytic graphite (HOPG) substrates has a crystal structure consistent with the β-phase.[47] The substrate, as well as the growth kinetics, is believed to play a critical role in the atomic structure of 2D tellurene, which

necessitates more efforts in promoting the theoretical understanding and the experimental investigation of 2D tellurene.

Many recent studies aimed to explore the electric band structure of tellurene. Qiao *et al.* reported that bilayer tellurene possessed an indirect bandgap of 1.17 eV in theoretical calculations. The bandgap will reduce with increasing layer numbers, reaching 0.31 eV for bulk tellurium.[91] Experimentally, monolayer tellurene grown on graphene is a p-type semiconductor with a bandgap of 0.92 eV, which is determined by dI/dV spectra from STS.[90] Tellurene also demonstrates high carrier mobility ranging from hundreds to thousands of $cm^2 V^{-1} s^{-1}$, depending on the thickness and synthetic methods.[89,92] In addition, the solution-grown tellurene possesses excellent chemical stability. Such tellurene-based field-effect transistors maintain the performance in air for more than two months.[93]

Other than tellurene, the successful synthesis of 2D selenene in group 16 is also reported recently.[48] However, there is little research on aspects of energy applications of selenene, which calls for further studies.

Above all, elemental 2D materials exhibit rich atomic structures, such as puckered structures for BP and black arsenene, and buckled structures for β-antimonene and grey arsenene. Moreover, different elemental 2D materials possess various electronic characteristics, including carrier mobility and tunable bandgap scope. Specifically, some elemental 2D materials (BP, arsenene, *etc.*) exhibit a direct band gap and high mobility, and demonstrate excellent application potential. In conclusion, the various atomic structures combined with the electronic characteristics of elemental 2D materials, facilitate their extensive applications in a variety of energy storage and conversion areas.

3. Synthetic approaches

Despite the significant synthetic challenges, a variety of reliable fabrication strategies have been developed to prepare elemental 2D materials with controlled crystal structures and morphologies. These novel synthetic methods can be classified into two main strategies, top-down methods (mechanical cleavage, liquid-phase exfoliation, and electrochemical exfoliation) and bottom-up methods (chemical vapor deposition and molecular beam epitaxy). In top-down methods, 2D materials are usually obtained by various exfoliation processes that break the weak van der Waals interaction between atomic layers. In comparison, bottom-up methods refer to the direct synthesis of monolayer to few-layer 2D materials through different chemical reactions in the gas or liquid phases.

3.1 Top-down methods

3.1.1 Mechanical exfoliation. Mechanical cleavage (Fig. 2a), widely known as the "scotch tape" method, was established by Novoselov and coworkers during their discovery of graphene,[94] causing a sensation in the field of 2D materials. The relatively large interaction between the substrate and materials breaks the weak van der Waals forces between atomic layers to produce 2D materials from few layers down to the monolayer limit. The Scotch tape method is successfully utilized to produce a variety of elemental 2D materials, such as BP,[95] antimonene,[96] arsenene[86] and bismuthene.[97] For example, few-layer black arsenene flakes have been obtained *via* mechanical exfoliation.[86] The minor step of 0.6 nm obtained in atomic force microscopic (AFM) characterization is consistent with the theoretical prediction. However, the manual selection process of mechanical exfoliation often takes a long time to obtain samples with a specific thickness and lateral dimension, and is highly dependent on the skill of operators. Moreover, it is limited to source crystals with clear layer structures. Thereby, although the mechanical exfoliation method is straightforward and generally applicable, it faces serious limitations in practical applications.

Notably, numerous modifications have emerged in recent studies to tackle these problems. For instance, a modified mechanical exfoliation method has been reported, capable of producing a wide range of 2D materials with a large lateral size.[98] It is achieved by adopting oxygen plasma treatment to remove ambient absorbents on the substrate prior to the exfoliation and additional heat treatment during the exfoliation to enhance the contact between bulk layered materials and the substrate. In addition, metal-assisted mechanical exfoliation has been developed to synthesize high-quality BP flakes efficiently.[99] With the assistance of the deposited gold/silver layer, the adhesive force between metal layers and bulk layered materials is significantly enhanced, resulting in enhanced production and increased product sizes.

3.1.2 Liquid-phase exfoliation. Liquid-phase exfoliation (LPE) has served as an efficient option to synthesize elemental 2D materials with facile procedures and high yield.[100,101] As shown in Fig. 2b, with the assistance of extensive sonication, the weak interlayer van der Waals forces of bulk layered materials can be broken in various solvents, including *N*-methyl pyrrolidone (NMP), isopropanol (IPA), dimethylformamide (DMF), water and their mixture. For example, few-layer BP could be prepared by employing a sealed-tip ultrasonication system with minimized BP decomposition.[102] After comparing products obtained in various solvents, NMP and DMF were found to be the most suitable solvents for BP exfoliation due to their relatively high boiling points and surface tension ($\sim$40 mJ m^{-2}).[103] Besides, a systematic study on exfoliation of antimonene has been presented from three aspects, including pre-processing, solvent selection and ultrasound parameters.[104] The results implied that various pre-processing procedures of antimonene, such as grinding, dry ball-milling and wet ball-milling, strongly affect both the yield and morphology of the final product. And the NMP/H_2O mixture was the superior solvent due to the matching surface energy. Although becoming increasingly popular, liquid exfoliation still faces critical weaknesses, such as large distributions of thickness, small lateral sizes, the toxicity of organic solvents, and, more importantly, its incapability to produce true atomic layers. In addition, the nanomaterials obtained from LPE are often a mixture of 2D nanosheets in different thicknesses and 0D quantum dots, which is not ideal for practical applications.

3.1.3 Electrochemical exfoliation. Electrochemical exfoliation (Fig. 2c) offers a fine balance between material quality and

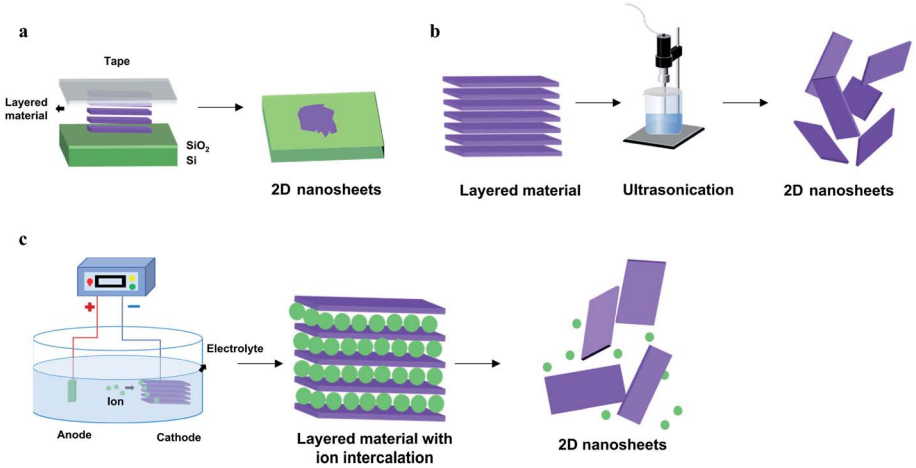

Fig. 2 Schematic illustration of top-down preparation methods of elemental 2D materials. (a) Mechanical exfoliation. (b) Liquid-phase exfoliation. (c) Electrochemical exfoliation.

production scalability. Exfoliation relies on ion insertion into atomic layers driven by the electrochemical potential to break the van der Waals interactions between the atomic layers. Electrochemical exfoliation can easily produce few-layer to monolayer nanosheets on a large scale. In addition, the quality of the exfoliated 2D nanosheets can be efficiently tuned by controlling various factors, including the size of the ions, physical properties of the solvents, the electrochemical potential and current density.[105] Metal cations are used in most cases, with some exceptions of anions such as SO_4^{2-} (ref. 106) and organic cations.[107–109] Naturally, electrochemical exfoliation is widely applied in the synthesis of elemental 2D materials.[105,110–113] For example, Wu and coworkers reported the production of few-layer bismuthene *via* electrochemical exfoliation.[107] The expanded interlayer distance of bismuthene after the tetraheptylammonium cation intercalation, combined with additional shear forces provided by ultrasonication, contributes to the efficient peeling of atomic layers. In addition, large-scale preparation of BP nanosheets *via* electrochemical exfoliation has recently been reported.[110,112] Moreover, β-antimonene can also be prepared *via* electrochemical intercalation from bulk β-antimony.[114,115]

In general, top-down approaches rely on the facile exfoliation process and are relatively cost-effective, however still facing various limitations. Mechanical exfoliation is severely restricted by its low yield, while the products obtained by liquid exfoliation often exhibit a small lateral size and a large distribution of thickness. Alternatively, electrochemical exfoliation is more efficient, highly controllable and mass productive. However, it is not applicable for all elemental 2D materials due to the difference in source crystals and the intercalation mechanism.

3.2 Bottom-up methods

Bottom-up methods refer to the direct synthesis of nanomaterials from precursors by chemical reactions, which generally produce high-quality 2D elemental materials in scale. In particular, due to the large energy and bonding configuration difference between bulk and 2D layered materials in groups 13 and 14, it is extremely difficult to exfoliate 2D layered structures from the bulk sources directly.[116] Bottom-up approaches are, therefore, favored.

3.2.1 Molecular beam epitaxy (MBE). MBE uses individual elements as precursors to epitaxially grow single-to-few atomic layers of 2D materials on metallic substrates with matching lattice constants. Among other advantages, MBE provides an exceptionally clean surface of the as-prepared materials, which can be further characterized or integrated into functional devices without contamination. Although MBE has been used to prepare antimonene,[117] and tellurene,[118] it really shines in the preparation of elemental 2D materials of groups 13 and 14.

As shown in Fig. 3a, the first successful synthesis of borophene was reported using MBE growth on a Ag(111) substrate.[15] In this experiment, a mixture of two borophene phases was observed, which were identified as striped and homogeneous phases, respectively. Almost at the same time, Feng *et al.* reported the synthesis of borophene by MBE in a parallel study.[20] When the substrate was changed to Au, besides the growth of few-layer nanosheets, borophene islands with a triangular structure and honeycomb lattice were also observed.[55] Interestingly, during the growth, borophene island discrete nanoclusters were initially observed before the formation of larger nanosheets with increasing boron coverage, resulting from the increasing boron dose. It is worth mentioning that elemental 2D materials with a honeycomb structure (for instance, graphene, silicene, germanene, and stanine) are favored in many applications due to the Dirac fermions and other exotic properties hosted by the highest lattice hole density among the typical lattice structures.[119,120] However, the energetical instability caused by electron deficiency of boron makes it challenging to synthesize a honeycomb structure, which is finally obtained on an Al(111) substrate using MBE under UHV conditions.[26] The small size (from several to hundreds of nanometers) of the obtained borophene on Ag, Al, or Au surfaces limits its detailed property

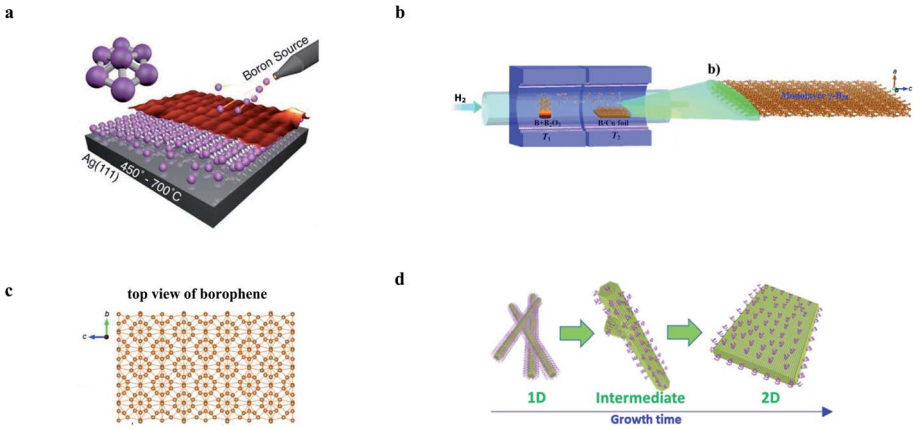

Fig. 3 Schematic illustration of bottom-up preparation methods of elemental 2D materials. (a) Diagram of molecular beam epitaxy (MBE) growth of Borophene on the Ag(111) substrate. Reproduced with permission,[14] AAAS. (b) Diagram of the homemade two-zone furnace for the chemical vapor deposition (CVD) growth of the borophene thin film on Cu foil.[17] (c) Schematic diagram of the prepared borophene from the top view in (b).[17] (b) and (c) Reproduced with permission,[17] Wiley-VCH. (d) Morphology evolution from 1D Te structures to 2D tellurene in the hydrothermal synthesis of tellurene. Reproduced with permission,[81] Springer Nature.

characterization and applications.[15,26] To this end, Wu *et al.* synthesized large-area borophene with a domain size of 10–100 μm^2 by diffusion of boron into copper, followed by repeated resurfacing and recrystallization processes.[29,30] Recently, Ir(111) was also used as the epitaxial substrate to produce large-area borophene.[28] Unlike earlier reported studies, the borophene formed a single phase (χ_6) in a wide range of experimental conditions.

In group 14, silicene has been successfully synthesized by epitaxial growth on different substrates such as Ag(111),[56,121–123] Ag(110),[124] MoS_2,[125] $ZrBr_2(0001)$,[126] Ir(111),[127] and Au(110)[128] at different temperatures and deposition rates. Due to the 3/4 ratio of lattice constants between Ag and Si, silver is the most appropriate substrate for the epitaxial growth of silicene among other substrates.[129,130] Many potential substrates to grow silicene have been predicted by theoretical calculations, such as aluminum nitride,[131,132] chalcogenide-layered compounds,[133] ZnS,[132] CaF_2,[134] and gallium dichalcogenides,[135] which are yet to be experimentally realized.

Germanene by MBE has been successfully fabricated on Au(111),[136] Al(111),[137] Pt(111),[138,139] and Cu(111).[140] Recently, a novel segregation method to synthesize large-scale germanene has been developed using a Ag(111) thin film epitaxially grown on as the substrate. Monolayer and multilayer stanene nanosheets were firstly obtained on a Bi_2Te_3 substrate by MBE, and the atomic and electronic structures of stanene were experimentally determined, which is consistent with the calculation results.[141] Later, MBE growth of stanene was demonstrated on Sb(111),[142] Ag(111),[39] and Cu(111)[39] substrates. Interestingly, it has been found in density-functional theory (DFT) calculations.[39] that various epilayer structures grown on Ag(111) might spontaneously recover to become a perfect stanene structure after departing from the substrate.

3.2.2 Chemical vapor deposition (CVD). CVD (Fig. 3b and c) is another widely adopted bottom-up growth method for the direct synthesis of high-quality 2D materials on both metal and dielectric substrates. Direct CVD growth of 2D materials on desired semiconducting or dielectric substrates (including Si, Ge, *etc.*) contributes to the transfer-free fabrication of devices, which not only ensures seamless contact but reduces the risk of contamination. However, aside from the relatively high cost, the main disadvantage of current CVD methods is the difficulty in introducing single nucleation, which leads to a small crystal domain size that could not meet the requirement in highly integrated devices.[143,144] CVD growth borophene has been realized on copper foil using a mixture of pure boron and boron oxide powders as the precursor.[18] The obtained borophene features an orthorhombic γ-B_{28} structure, consisting of B_{12} units and B_2 dumbbells. Additionally, a BP film has been successfully prepared *via* the CVD method by transforming a red phosphorus (RP) film at a high temperature or pressure.[145,146] For example, Xia and coworkers prepared a large-scale BP thin film with continuous lengths up to 600 μm on 5 mm sapphire substrates *via* this conversion strategy at an elevated temperature (700 °C) and pressure (1.5 Gpa).[145] Furthermore, antimonene has been synthesized by the CVD method on SiO_2 substrates, with a very thin thickness (ranging from ~0.73 nm to ~23.3 nm) and large area (nearly 40 μm^2).[76] Besides, α-phase tellurene has also been realized on mica substrates by the CVD method.[147] In general, the electronic and optical properties of CVD-grown thin films of elemental 2D materials are hampered due to abundant grain boundaries and defects. Moving forward, the further development of CVD methods for the growth of high-quality thin films is critical for the broad applications of elemental 2D materials.

3.2.3 Wet chemistry approaches. Wet chemistry approaches, such as hydrothermal and solvent-thermal methods, directly synthesize nanomaterials *via* nucleation and growth processes in precursor solutions at a high temperature and/or high pressure. The lateral size and morphology are controlled by many factors, including the ratio of precursors, the pH value of the reaction system, the reaction time, and the

temperature.[148] Although widely used in the high-yield synthesis of 2D materials, wet-chemical synthesis found limited success in elemental 2D materials (tellurene,[89,149] antimonene,[150] and bismuthene[151]). Few-layer tellurene nanosheets could be obtained through the reduction of sodium tellurite (Na_2TeO_3) by hydrazine hydrate (N_2H_4) in an alkaline solution, with the assistance of the polyvinylpyrrolidone (PVP) ligand.[152] The growth mechanism study (Fig. 3d) demonstrates that the PVP blocks the growth of crystal-face-blocking, resulting in the formation of 2D structures. Specifically, during the initial growth, PVP is inclined to adsorb on the $\{10\bar{1}0\}$ facet of the nucleated seeds, thereby leading to the formation of the 1D structure. As the growth continues, PVP is insufficient to cover the crystal plane, hence significantly enhances the growth of $\{10\bar{1}0\}$ surfaces along the $\{1\bar{2}10\}$ direction, which contributes to the formation of the 2D morphology of tellurene. In addition, few-layer hexagonal antimonene nanosheets have been prepared *via* a facile colloidal synthesis method.[150] The XRD characterization of the final product confirmed the identity of the rhombohedral phase (β-antimonene) without impurities. Bismuthene has also been synthesized *via* the hydrothermal method by reduction of the precursor $Bi_2O_2CO_3$.[153] Moreover, a one-step wet-chemistry method has been developed to prepare bismuthene with an average thickness of 0.6 nm,[151] based on the simple reduction of $BiCl_3$ by $NaBH_4$.

3.2.4 Other "bottom-up" methods. In addition to MBE, CVD and wet chemistry methods, there are some other "bottom-up" strategies that have found success in the synthesis of 2D elemental materials, such as electrochemical formation for germanene,[154] van der Waals epitaxy for arsenene[84] and antimonene,[155] pulsed laser deposition for 2D bismuthene,[78] and physical vapor deposition for tellurene.[156]

In "bottom-up" methods, elemental 2D materials are constructed from atomic or molecular precursors. Compared with "top-down" methods, "bottom-up" methods can break the requirements of layered source crystals and achieve reasonable yield. However, "bottom-up" methods such as the commonly used MBE and CVD, heavily rely on the chemical bonds/interactions between precursors and substrates, and therefore are usually limited to the lattice symmetry and parameters. Further development calls for more exploration into the combination of precursors, substrates and deposition conditions. In addition, most wet-chemistry methods are only acceptable for specific nanoscale materials with uncontrollable sizes. It is particularly difficult to obtain elemental 2D materials in a monolayer *via* wet-chemistry approaches. And the surfactants resulting from the synthesis process are undesirable in the consequent applications. Overall, it is still challenging to find general, effective, high-yield and low-cost methods for the controllable synthesis of 2D materials.

4. Applications in energy storage

4.1 Batteries

The majority of applications of elemental 2D materials in energy storage fields are utilization as electrode materials for batteries, including Li-ion batteries (LIB), Na-ion batteries (SIB), Li–sulfur batteries (LSB), and other next-generation batteries.

4.1.1 Li-ion batteries and Na-ion batteries. As a new family of 2D materials, elemental 2D materials exhibit many advantages, such as large carrier mobility, large theoretical volumes, and moderate layer distances, which make them particularly suitable for LIB and SIB. Several theoretical studies have explored the potential of elemental 2D materials, including few-layer BP,[157] borophene,[158] antimonene,[74] bismuthene,[159] silicene,[160] stanene[160] and arsenene,[161] respectively, in energy storage along with their working principles. The migration paths for Li/Na ion diffusion and the lithiated/sodiated structures of some elemental 2D materials are summarized in Fig. 4.

The diffusion behavior of Li in few-layer BP has received the most attention.[43,157] Notably, few-layer BP shows a puckered lattice structure and a large interlayer distance of 0.53 nm, providing a suitable interlayer channel for the ion insertion/extraction.[162] BP can be intercalated with three Li ions at the end of the lithiation stage to form the Li_3P phase and thereby possesses a high theoretical volume of 2596 mA h g^{-1}. It has a multistep lithiation process: BP → LiP → Li_2P → Li_3P. Additionally, theoretical results demonstrate a strong diffusion anisotropy, with a lower energy barrier (0.08 eV) along the zigzag direction, compared with the high energy barrier (0.68 eV) along the armchair direction.[157] The shallow energy barrier along the zigzag direction implies ultrahigh Li diffusivity, which is 10^2 times faster than that on MoS_2 or 10^4 times faster than that on graphene. Such highly anticipated anisotropy has been experimentally realized.[163]

The potential of borophene as an anode material for metal-ion batteries is also investigated *via* first-principles calculations. At full lithium insertion forming $Li_{0.75}B$, borophene possesses a high theoretical specific capacity of 1860 mA h g^{-1}.[158,164] Similar to BP, borophene also exhibits a strong Li diffusion anisotropy, *i.e.*, the energy barrier for Li diffusion is only 2.6 meV along the furrow direction of corrugated borophene, much lower than that of the perpendicular direction (325.1 meV).[158]

In addition, the sodiation/desodiation mechanism of antimonene is researched based on DFT calculations, along with experimental characterization, including *in situ* synchrotron X-ray diffraction (XRD) and *ex situ* selected-area electron diffraction (SAED).[74,165] Antimonene has a theoretical capacity of 660 mA h g^{-1} for SIB, with reversible crystalline phase evolution (Sb → NaSb → Na_3Sb) during the ion insertion/extraction process, which is verified by the experimental characterization. Additionally, antimonene showed anisotropic volume expansion along the ***a***/***b*** plane in the Na ion intercalation process.[74] This can be explained by the lower Na-ion diffusion barrier of 0.14 eV, enabling fast sodiation reaction kinetics and excellent cyclic performance for SIB.

Similarly, first-principles calculations are implemented to explore few-layer bismuthene in LIB and SIB.[166] The calculated results demonstrated that bismuthene possessed high theoretical storage capacities of 2276 mA h g^{-1} and 2149 mA h g^{-1} for Li and Na, respectively. The sodiation storage mechanism in bismuthene is also experimentally verified by *in situ* TEM with a multistep crystal phase evolution (Fig. 4a), Bi → NaBi →

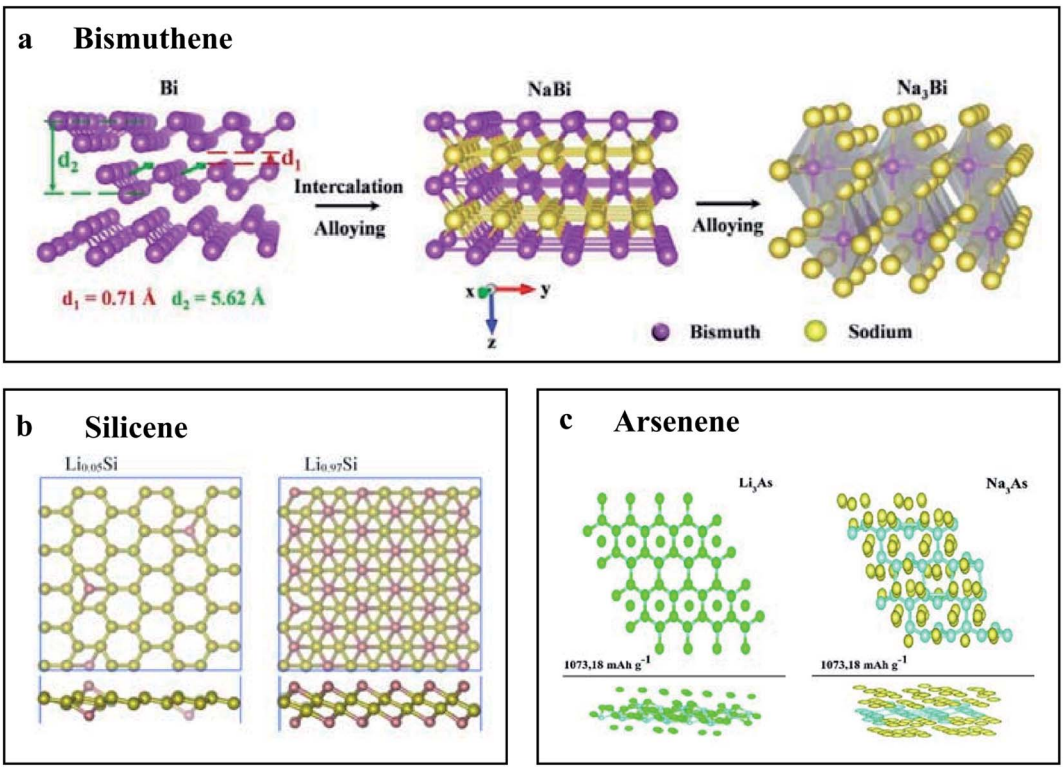

Fig. 4 Schematic diagram of structure evolution of elemental 2D materials during the operation of a Li-ion battery and Na-ion battery. (a) Schematics of structural evolution of bismuthene to Na_3Bi *via* NaBi during electrochemical sodiation. Reproduced with permission,[68] Wiley-VCH. (b) Structures of lithiated silicene. Reproduced with permission,[153] Elsevier. (c) Top and side views of the fully relaxed structures of Li_xAs and Na_xAs. Reproduced with permission,[154] Royal Society of Chemistry.

Na_3Bi, accompanied by a large anisotropic volume expansion of 142% occurring mainly along the *z*-axis.[45]

Furthermore, silicene, germanene and stanene are predicted to possess theoretical capacities of 954 mA h g^{-1}, 369 mA h g^{-1} and 226 mA h g^{-1} for both Li or Na ions storage, respectively (Fig. 4b).[160] In addition, theoretical results of monolayer arsenene as the anode for (Li/Na/Mg)-ion batteries, as shown in Fig. 4c, demonstrates that monolayer arsenene possesses a high theoretical capacity of 1609.77 mA h g^{-1} for Li, 1073.18 mA h g^{-1} for Na, and 1430.91 mA h g^{-1} for Mg.[161]

Inspired by the progress in theoretical calculations and the rapid development of synthetic methods, extensive experimental studies have been carried out to determine the potential of emerging elemental 2D materials as an anode in LIB and SIB.

Due to the high theoretical volume and good ion diffusivity, BP is the most researched elemental 2D material for use as a battery anode and probably one of the most promising ones, demonstrating high capacity up to ~2000 mA h g^{-1},[68] which is far beyond those of other 2D anode materials for LIB or SIB, such as MXene.[167] Still, the main drawback of BP in the electrochemical process involves the huge volume change and the destruction of the crystal structure, which lead to lower coulombic efficiency (≈8%) and unsatisfactory reversible specific capacity in the following cycles.[168] To deal with these problems, researchers have made extensive efforts to composite BP with other functional materials to enhance its mechanical strength. In one good example, few-layer BP nanosheets were sandwiched between graphene layers to form a composite SIB anode, exhibiting an ultrahigh specific capacity of 2440 mA h g^{-1} at a current density of 0.05 A g^{-1} along with good cycling performance.[163] The graphene layers not only enhance the electrical conductivity but also provide mechanical support to accommodate the sizeable anisotropic expansion of phosphorene layers along the *y* and *z* axial directions, which is further verified by *in situ* TEM characterization. Similarly, BP–graphene (BP–G) hybrid paper was fabricated by vacuum filtration of a mixed dispersion containing graphene and BP, demonstrating a high electrical conductivity(about 1000 S cm^{-1}) and excellent flexibility.[169] As a result, the LIB showed a high specific capacity of 501 mA h g^{-1}, good rate capability, and prolonged cycling performance with a capacity retention of 80.2% at a current density of 500 mA g^{-1} after 500 cycles.

Beyond BP, few-layer antimonene nanosheets prepared *via* the LPE method have also been used as anode materials in Li-ion batteries.[165] As illustrated in Fig. 5a and b, antimonene nanosheets exhibited better cycling performance and rate capability than bulk antimony and antimony nanoparticles derived from similar LPE process. Based on the first-principles calculation, antimonene exhibited a minimal Li^+ ion diffusion barrier of 0.25 eV along the in-plane channel, whereas the Li-ion diffusion across layers required a larger energy barrier of 1.14 eV. Thereby, antimonene with a large lateral size facilitated the

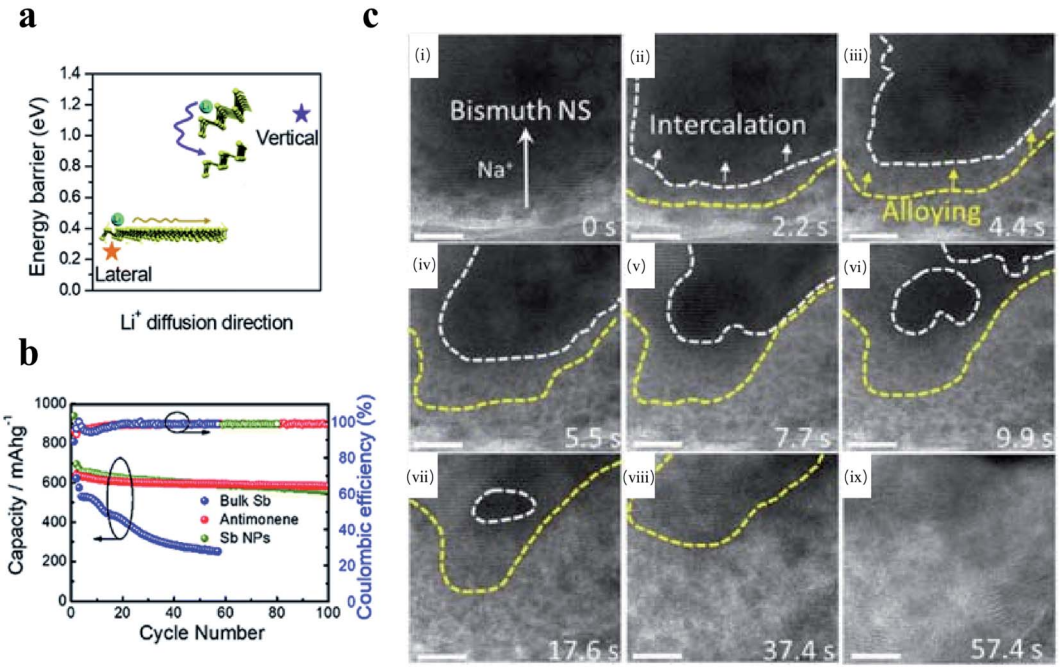

Fig. 5 (a) and (b) the electrochemical performance of antimonene in Li-ion battery.[158] (a) Schematic diagram of the Li ion diffusion barrier in antimonene. (b) Cycling performances of the anode made of bulk β-phase antimony, antimonene nanosheets, and antimony nanoparticles in a Li-ion battery. (a) and (b) Reproduced with permission,[158] Royal Society of Chemistry. (c) (i)–(ix) are time-sequences HR-TEM images of bismuthene nanosheets during the sodiation process in a Na-ion battery. Scale bar: 10 nm. Reproduced with permission,[152] American Chemical Society.

ion insertion process and enhanced Li-ion storage compared with bulk antimony and antimony nanoparticles. Besides, ultrathin bismuthene nanosheets were prepared with a similar LPE method and used as an anode for SIB.[159] Notably, the time-sequences of high-resolution transmission electron microscope (HRTEM) images in Fig. 5c indicate that the intercalation of Na ions does not collapse the crystal structure of 2D bismuthene. Moreover, after four cycles in the *in situ* TEM study, bismuthene nanosheets showed a small lateral expansion of around 13% and exhibited a superior cyclic ability after 200 cycles compared with the bulk counterpart.

4.1.2 Li–sulfur battery. LSB are considered as one of the most promising next-generation rechargeable batteries due to their high theoretical energy density. Thery are, however, largely limited by the insulating nature of sulfur as well as the material loss during operation as a result of the dissolution of soluble lithium polysulfides.[170]

To overcome this polysulfide dissolution, a novel BP functionalized separator was utilized in LSB, showing much enhanced specific capacity and cycling performance compared to the commercial polypropylene separator.[171] According to first-principles calculations, BP exhibits a high binding energy with various lithium polysulfide/sulfide species and thereby provides strong adsorption of lithium polysulfide/sulfide species to suppress the "shuttle effect". Hence, the functionalized separator can effectively reduce material loss and improve the electrochemical performance of LSB.

In another theoretical study, the potential of borophene to serve as a good host of cathode materials for LSB[172,173] was investigated. The puckered lattice structure is expected to contribute to an ultrahigh adsorption ability towards lithium polysulfides. However, it also suggested that the lithium polysulfides could decompose on borophene with no energy barrier, leading to the separation of lithium and sulfur and therefore undesirable sulfur loss during charge–discharge cycles.[173] In contrast, defective borophene demonstrates moderate adsorption energy toward lithium polysulfides, which can not only efficiently anchor lithium polysulfides to suppress the "shuttle effect", but also avoid the dissolution of sulfur materials.

4.1.3 Other types of batteries. Elemental 2D materials also show potential in other next-generation rechargeable batteries. For example, a novel conversion-type aqueous Zn–Te battery has been proposed and fabricated recently.[174] The Zn–Te battery adopted tellurene nanosheets prepared by the LPE method as the cathode, Zn as the anode, and 1 M $ZnSO_4$ in H_2O as the electrolyte. As shown in Fig. 6a and b, galvanostatic cycling with potential limitation indicates that tellurene exhibits a high capacity of 2619 mA h cm^{-3} (419 mA h g^{-1}) at 0.05 A g^{-1}, which is much higher than that of bulk Te (1699 mA h cm^{-3}), approaching the theoretical limit. The conversion-type ion storage behavior is one of the main reasons for such ultrahigh capacity. The high capacity is also attributed to the high intrinsic conductivity of tellurene (2×10^2 S m^{-1}), the two-dimension morphology, and the high interlayer distance of 3.48 Å. Additionally, the tellurene electrode exhibits a high capacity retention of 82.8% after 500 cycles and an impressive coulombic efficiency of near 100%, which is ascribed to the immunization to the "shuttle effect", due to the insolubility of discharge

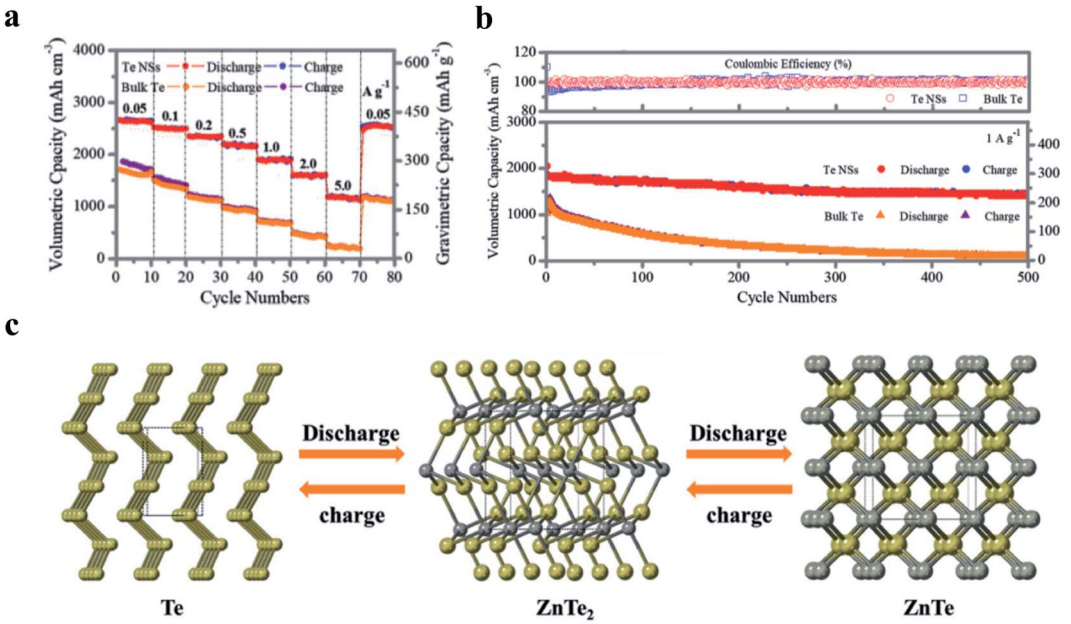

Fig. 6 Tellurene as an anode for high-performance Zn–Te batteries. (a) Rate performance based on different current densities from 0.05 to 5 A g^{-1}. (b) Cycling performance and coulombic efficiency of Te NSs and bulk Te at 1 A g^{-1}. (c) Schematic representation for phase transformation during the discharging process (yellow: Te atoms, gray: Zn atoms). Reproduced with permission,[167] Wiley-VCH.

products ($ZnTe_2$ and ZnTe) in aqueous electrolytes. Additionally, the *ex situ* XRD characterization results indicate that the discharge process involves the successive phase transitions (Fig. 6c) from hexagonal-phase tellurene to trigonal-phase $ZnTe_2$ (intermitted product) and eventually to cubic-phase ZnTe (final product), resulting in a long and ultra-flat discharge plateau.

4.2 Supercapacitor

Supercapacitors are an electrochemical energy storage device that can provide higher power density than batteries as well as higher energy density than conventional dielectric capacitors.[175] The large surface area, large interlayer spacing and high carrier mobility make elemental 2D materials promising electrode materials for supercapacitors. For example, a free-standing polypyrrole (PPy)/BP film was prepared *via* a facile electrodeposition method and served as a supercapacitor electrode.[176] BP nanosheets efficiently suppress the disordered packing of PPy during electrodeposition, thereby facilitating ion diffusion and electron transport as well as enhancing stability during the electrochemical processes. The hybrid electrode exhibits a high capacitive value of 497.5 F g^{-1} and good cycling performance. A highly flexible supercapacitor was assembled based on the PPy/BP composite film, showing great potential for a variety of electronics. In this work, thin BP nanosheets (fewer than five layers), *via* the LPE method, are hybridized with graphene nanosheets to form the BP/graphene film through vacuum filtration, which was further transformed into an oxidized free-standing black phosphorus (oBP)/reduced graphene oxide (rGO) hybrid film (oBP/rGO, Fig. 7a and b) *via* controlled ozonation and subsequent thermal treatment.[177] As is shown in Fig. 7c, the free-standing BP/rGO hybrid film exhibited enhanced electrochemical performance in a supercapacitor compared with BP and graphene, with a high specific capacitance of 478 F g^{-1} at 1 A g^{-1} (four times greater than that of black phosphorus) and good rate capability. The specific capacitance of the BP/rGO hybrid film is higher than those of electrodes based on other 2D materials, *e.g.*, conductive 2D titanium carbide, which possesses a specific capacitance of 245 F g^{-1} at a scan rate of 2 mV s^{-1}.[178] Based on DFT calculations and experimental characterization, such as *in situ* Raman spectroelectrochemical spectra studies, it is evident that the molecular-level redox-active P=O sites obtained from controlled ozone-driven oxidation provide more active sites for proton accumulation and lead to the high specific capacitance. Additionally, hybridizing BP with electronically conductive rGO results in a high electronic conductivity, which is favorable to the rate capability.

Besides, antimonene also serves as a promising electrode material for supercapacitors.[179] Few-layer antimonene demonstrates remarkable electrochemical performance in supercapacitors with a capacitance of 1578 F g^{-1}, which implied high charge storage capacity and could be attributed to 2D layered atomic structure as well as the high intrinsic pseudocapacitive activity of antimonene.[180] However, although the high capacitance of antimonene was confirmed by follow-up research studies,[181,182] the mechanism for the high intrinsic pseudocapacitive activity of antimonene requires further investigation. The assembled device shows very competitive performance with energy and power densities of 20 mW h kg^{-1} and 4.8 kW kg^{-1}, respectively. Additionally, antimonene was also hybridized with other active materials or conductive substrates to enhance electrochemical performance. For example, an antimonene/3D-

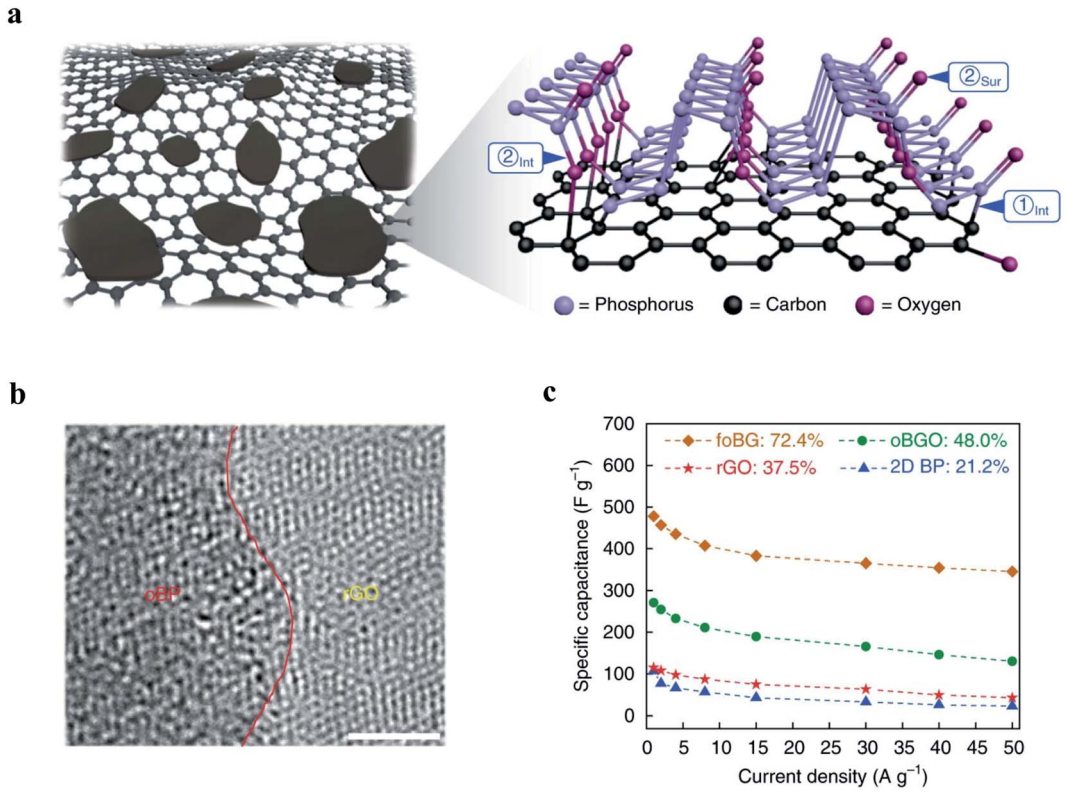

Fig. 7 Supercapacitor based on the hybrid structure of oxidized black phosphorus (oBP) and a reduced graphene oxide film (oBP/rGO).[170] (a) Illustration of the schematic model of the oBP/rGO hybrid film. (b) Cross-sectional-view HR-TEM image of the free-standing oBP/rGO hybrid film, showing the heterointerface of the oBP/rGO hybrid film. Scale bar, 1 nm. (c) Rate capability of 2D BP, rGO, oBP/GO and free-standing oBG/rGO (foBG) at various current densities from 1 to 50 A g^{-1}. 2D BP: black phosphorene; rGO: reduced graphene oxide; oBP/GO: oBP and graphene oxide hybrid film; oBP/rGO: oBP and reduced graphene oxide hybrid film. Reproduced with permission,[170] Springer Nature.

Ni foam hybrid electrode demonstrates an ultrahigh specific capacity of 1618.41 mA h g^{-1} (~6854.45 F g^{-1}) at a low scan rate of 5 mV s^{-1}.[182] Recently, the novel VS_4/antimonene composite electrode also exhibited excellent electrochemical performance for supercapacitors.[183] The hybridization of VS_4 with highly electroactive few-layer antimonene (4–6 layers) significantly increased the number of active surface sites owing to the synergistic combination of two highly pseudocapacitive materials. The VS_4/antimonene showed a specific capacitance of 1447 F g^{-1} at 6 A g^{-1} and good rate capability, that it retains 782.1 F g^{-1} at a large current density of 30 A g^{-1}. And the VS_4/antimonene||VS_4/antimonene symmetry supercapacitor demonstrated high specific capacitance (539.4 F g^{-1}@3 A g^{-1}), excellent cycling stability (174% after 10 000 cycles), and high energy and power density (93.5 W h kg^{-1} and 1705 W kg^{-1}).

5. Applications in electrocatalysis

Recently, there have been rapid theoretical and experimental developments of elemental 2D materials in electrocatalytic reactions, including the hydrogen evolution reaction (HER), oxygen evolution reaction (OER), oxygen reduction reaction (ORR), carbon dioxide reduction (CO_2RR), and N_2 reduction reaction (NRR).

5.1 Water splitting

Water splitting involves the hydrogen evolution reaction (HER) at the cathode and the oxygen evolution reaction (OER) at the anode, respectively, in an electrolytic cell. Borophene,[184,185] antimonene,[104,186] black arsenene[187] and BP[188] have been reported as electrocatalysts for the electrocatalytic HER or OER.

BP has been considered to be a promising electrocatalyst for water splitting. However, plain BP exhibits instability and limited electrochemical performance, which is possibly caused by either a low density of catalytic sites or a limited electrical conductivity.[188] Thereby, composite materials based on BP and other nanomaterials are commonly used as high-performance electrocatalysts for water splitting. For example, BP was prepared by LPE and formed a heterostructure with N-doped graphene (NG) by sonication to serve as an electrocatalyst for overall water splitting.[188] The heterostructure electrocatalyst exhibited good electrochemical performance with a low cell voltage of 1.54 V at 10 mA cm^{-2} for overall water splitting in 1 M KOH solution, outperforming the integrated Pt/C@RuO_2 couple (1.60 V). It is believed that directional interfacial electron transfer induced by different Fermi levels between BP and NG not only enriched the electron density, but also optimized H adsorption/desorption to promote the HER, as well as enhanced the favorable formation of key OER intermediates (OOH*) to

improve the OER. In addition, few-layer antimonene nanosheets were prepared by LPE and utilized as bifunctional electrocatalysts for the HER and OER.[186] Both the HER and OER catalytic performance of few-layer antimonene nanosheets without any treatment showed great potential in the application of overall water splitting under alkaline conditions. Antimonene nanosheets have demonstrated an overpotential of 666 mV to achieve the current density of 1 mA cm^{-2} and a relatively large Tafel slope of 217.2 mV dec^{-1} in 1 M KOH solution in the HER. Also, it showed a moderate OER performance with a Tafel slope of 261.3 mV dec^{-1} and long-term stability in alkaline KOH solution for bifunctional water splitting, *i.e.*, both the HER and OER.

Furthermore, researchers have also forecasted the electrocatalysis performance of some elemental 2D materials *via* theoretical calculations. The metallic band structure and the multiple active sites of borophene make it promising in the HER.[20] The borophene electrocatalyst is expected to show an ultralow overpotential due to the small free energy of hydrogen adsorption (ΔG_H) of the β_{12}, α, and β_1 phases of borophene. Additionally, as reported by Feng and coworkers, pure black arsenene is unfavorable for the HER process due to the extremely weak binding strength of the hydrogen atom on its surface. However, the embedded O atoms at the surface of arsenene are expected to increase the binding strength of H to an appropriate degree and greatly improve the catalytic performance of black arsenene for the HER.[187]

Although some elemental 2D materials are inherently unfavorable for catalysis, they demonstrate potential as supporting substrates in some cases, which can be attributed to many of their unique characteristics.[189,190] Like most 2D materials, elemental 2D materials provide high surface areas, which are beneficial to the uniform dispersion of nanomaterials on the substrates. Additionally, elemental 2D materials often possess a high carrier concentration or large carrier mobility, which significantly facilitate charge transport in composite catalysts. Moreover, the various synergistic effects between substrates and nanomaterials on them could effectively enhance electrocatalytic activity. For example, a modified LPE process was reported to fabricate few-layer antimonene nanosheets while simultaneously growing RuS_2 nanodots on the antimonene during the LPE process, as shown in Fig. 8a.[189] The Ru–S–Sb/antimonene composite exhibits moderate HER performance with a low overpotential of 153 mV at a current density of 10 mA cm^{-2} (Fig. 8b) and a small Tafel slope of 118 mV dec^{-1} in 1.0 M phosphate-buffered saline (Fig. 8c). In addition, the catalytic performance of various single transition metal (TM) atoms supported on borophene with vacancies (denoted as the TM-BH system) has been investigated for the electrocatalytic ORR and OER.[190] Among them, Fe supported on borophene (Fe-BH) and Rh supported on borophene (Rh-BH) are two promising ORR catalysts with overpotentials of 430 mV and 470 mV, respectively. Furthermore, the Rh-BH also shows impressive OER performance with the overpotential of 240 mV, which is smaller than that of commercial RuO_2 by near 370 mV. Shi *et al.* also developed an electrocatalyst based on cobalt or Co_3O_4 nanoparticles decorated on BP nanosheets, exhibiting a low overpotential and excellent stability in the OER in alkaline media.[191]

5.2 CO_2 reduction reaction (CO_2RR) and N_2 reduction reaction (NRR)

Elemental 2D material-based electrocatalysts have attracted numberous research interest for the CO_2RR and NRR. For instance, the active orbital and electrons of the zigzag and diff-zigzag type edges of few-layer BP enable selective electrocatalysis of N_2 to NH_3,[192] achieving a high ammonia yield of 31.37 μg h^{-1} mg^{-1}_{cat}. Further study on few-layer antimonene electrocatalysts has reported an impressive NH_3 yield of 180.4 μg h^{-1} mg^{-1}_{cat} and faradaic efficiency of 11.6% when tested in 0.1 M KOH under ambient conditions.[193] In addition, bismuthene electrocatalysts also demonstrated efficient NH_3 production.[194,195]

The Li group reported the synthesis of free-standing bismuthene nanosheets (Fig. 8d and e) with a thickness of ~8.7 nm *via in situ* topotactic transformation of bismuth oxyiodide and used as a electrocatalyst in the CO_2RR. As is illustrated in Fig. 8f and g, bismuthene nanosheets demonstrated a cathodic current onset at approximately −1.3 V *versus* SCE in CO_2-saturated 0.5 M $NaHCO_3$ solution,[196] which increased to 11 mA cm^{-2} at −1.5 V *versus* SCE. And the initial faradaic efficiency was 16% at ~−1.3 V, which quickly rose to >95% at −1.5 V and maintained close to 100% until reaching −1.7 V. Bismuthene nanosheets showed good performance with high selectivity (~100% for formate formation) and FE_{HCOO^-} (up to 98%) at an overpotential of −580 mV as well as good cycling performance and an ultrasmall onset overpotential of <90 mV. Additionally, based on DFT calculations, borophene was also predicted as a promising catalyst for the CO_2RR due to its great capture capacity of CO_2,[197,198] although yet to be experimentally proven. Additionally, borophene has also been theoretically studied as the supporting substrate for Cu atomic chains as an electrocatalyst for the CO_2RR.[199] Based on first-principles calculations, the unique chain structures of Cu atoms played a key role in lowering the overpotential of the CO_2RR, implying great catalytic abilities of Cu-supported borophene for CO_2RR. Furthermore, silicene on Ag(111) was predicted to show good catalytic activity for CO_2 hydrogenation, which could be selectively controlled by the number of layers.[200] Based on the binding energy with the reaction intermediates, the supported silicene monolayer is expected to be favorable to form carbon monoxide, formic acid, and formaldehyde, while few-layer silicene is expected to form methanol and methane.

6. Applications in photocatalysis

Photocatalysis directly converts solar energy to chemical energy,[201,202] which could be an effective approach to overcome the intermittent nature of solar illumination in renewable energy production. The large surface area as well as the tunable bandgap, endows elemental 2D materials with great potential to serve as efficient photocatalysts. Recently, many theoretical

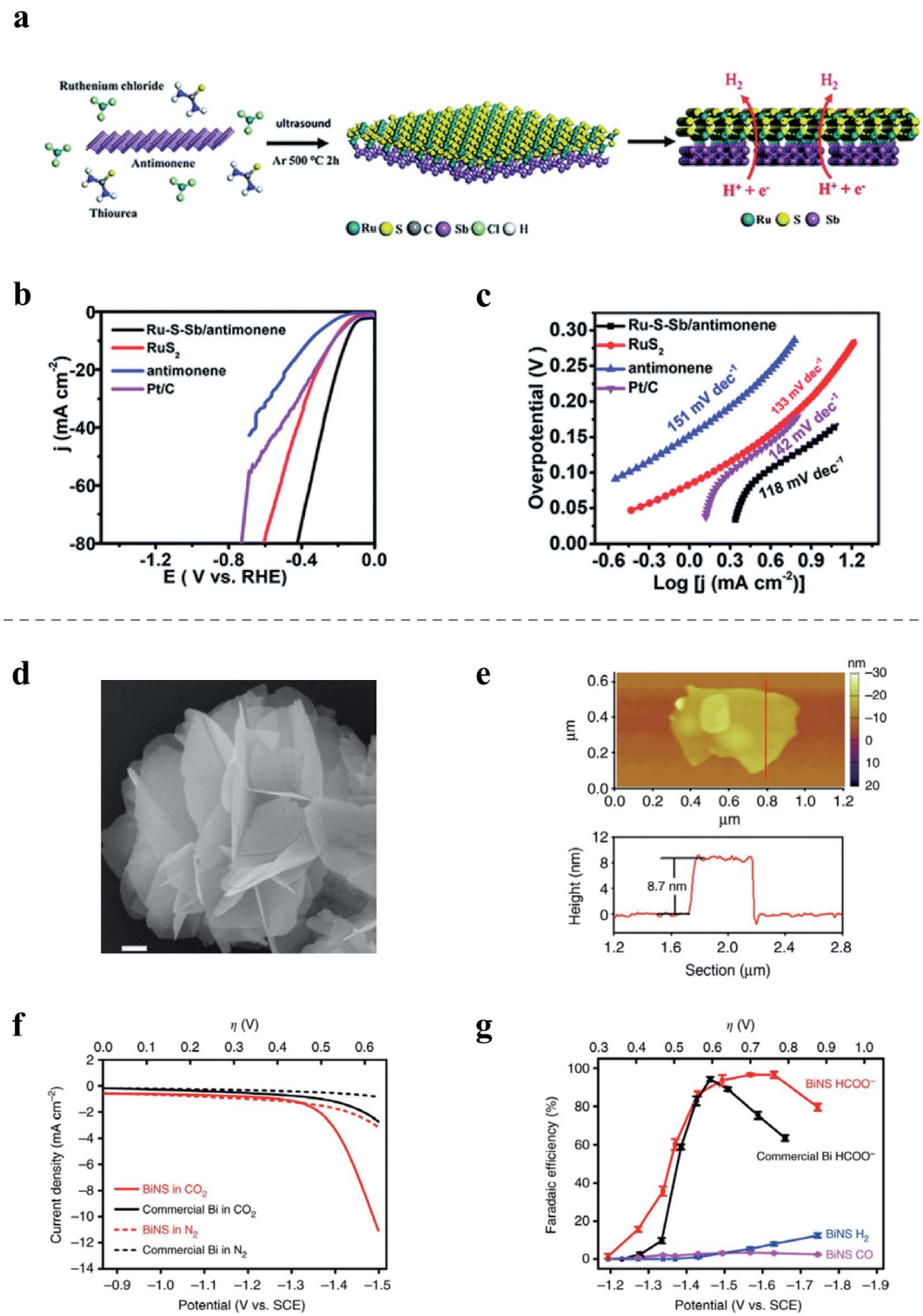

Fig. 8 (a–c) Preparation diagram and electrochemical performance of Ru−−S−−Sb/antimonene[180] for the HER: (a) schematic of the preparation of Ru–S–Sb/antimonene; (b) polarization curves at 5 mV s^{-1} in the electrolyte; (c) Tafel plots of Ru–S–Sb/antimonene, RuS nanodots, antimonene nanosheets and commercial Pt/C. (d–g) Characterization and electrochemical performance of free-standing bismuthene nanosheets[144] in the CO_2RR: (d) SEM image of bismuthene nanosheets, scale bar, 200 nm; (e) AFM image and the corresponding height profile of the bismuthene nanosheet; (f) polarization curves of bismuthene nanosheets (BiNS) and a commercial Bi nanopowder in N_2- or CO_2-saturated 0.5 M $NaHCO_3$; (g) potential-dependent faradaic efficiencies of $HCOO^-$, CO, and H_2 on BiNS in comparison with the faradaic efficiency of $HCOO^-$ on the commercial Bi nanopowder. (a–c) Reproduced with permission,[180] Royal Society of Chemistry. (d–g) Reproduced with permission,[144] Springer Nature.

calculation results have predicted potential interest for some emerging elemental 2D semiconductors as photocatalysts, including BP,[203] blue phosphorene,[204,205] violet phosphorene,[206] antimonene,[207,208] and arsenene.[209–211] However, the experimental realization is still limited, with most of the advances focusing on BP and its composite.

6.1 Photocatalytic hydrogen production

Few-layer BP is one of the most promising candidates for photocatalytic water splitting among elemental 2D materials, owing to its suitable conduction band (CB) position for hydrogen production and tunable bandgaps that can accommodate a wide range of photon absorption from ultraviolet to near-infrared. However, the practical application of BP in photocatalysis is primarily limited by the low stability and rapid recombination of photoinduced charge carriers, possibly related to its relatively narrow bandgap.[212] Constructing semiconductor heterostructures of elemental 2D materials and semiconductors is an effective approach to suppress charge carrier recombination, accelerate carrier mobility, and consequently enhance photocatalytic performance.[213–216] For example, the Z-scheme heterostructure strategy is often adopted to construct preferable band alignment to reduce the recombination of photoinduced charge carriers.[217] When the photocatalytic reaction happens in a Z-scheme band alignment, the photogenerated electrons in one semiconductor with lower reduction ability recombine with the photogenerated holes in the other semiconductor with a lower oxidation ability. Therefore, the photogenerated electrons in a semiconductor with high reduction ability and photogenerated holes with high oxidation ability can avoid recombination and participate in the photocatalytic reaction. As illustrated in Fig. 9a, a Z-scheme 2D/2D heterojunction of BP/Bi_2WO_6 was prepared by sonication treatment of the mixture solution of BP and monolayer Bi_2WO_6 nanosheets and used as a photocatalyst in both photocatalytic water splitting and NO removal.[218] The heterostructure photocatalyst exhibits a high H_2 evolution rate of 21 042 μmol g^{-1}, which is 9.15 times higher than that of pristine monolayer Bi_2WO_6 and also higher than that of other previously reported 2D photocatalysts, such as WS_2/CdS heterostructures, which demonstrated a photocatalytic HER performance of ~4200 μmol g^{-1} h^{-1}.[219] Similarly, the NO removal ratio is up to 67%, which is as high as 2.6 times that of pure monolayer Bi_2WO_6. 5,5-dimethyl-1-pyrroline-*N*-oxide (DMPO)-electron spin resonance spectroscopy (ESR) was utilized to track active radicals during the photodegradation process and proved the Z-scheme charge transfer mechanism. The electrons in the CB of Bi_2WO_6 combine with the holes in the valence band (VB) of BP. Consequently, the photoinduced electrons remain in the CB of BP to produce H_2 while the holes remain in the VB of Bi_2WO_6 to oxidize NO, as illustrated in Fig. 9b.

Furthermore, recent studies also show the potential of tellurene in photocatalytic H_2 generation. As shown in Fig. 9c, tellurene nanosheets were functionalized with single atomic cobalt species (ACS) and used as a catalyst for photocatalytic H_2 production.[220] The ACS functionalized tellurene nanosheets (denoted as Te NS-ACS) demonstrated a H_2 evolution rate of 130.8 μmol h^{-1} under visible light irradiation (Fig. 9d), with Eosin Y (EY) as a light absorber and triethanolamine (TEOA) as the sacrificial agent. The boosted electrochemical performance could be attributed to coordination between Te nanosheets and atomic cobalt, which altered the electronica structure and introduced intermediate energy states. As displayed in Fig. 9e, the intermediate energy states could act as trap sites to accommodate the photogenerated electrons, promoting charge separation and transfer. Qiu and coworkers prepared ultrathin 2D tellurene nanosheets (2–5 nm) *via* the LPE method and fabricated a tellurene/CdS heterostructure as a high-performance photocatalyst for photocatalytic hydrogen evolution.[221] The tellurene/CdS heterostructure exhibits an enhanced hydrogen production rate of 234.4 μmol h^{-1}, which is 7.8 times higher than that of bare CdS (30.2 μmol h^{-1}). Remarkably, the heterostructure photocatalyst maintained a stable photocatalytic H_2 production for more than 10 h. DFT calculation and time-resolved photoluminescence decay spectra spectroscopy suggested that the photoinduced electrons transfer from CdS to tellurene to produce H_2 rapidly. The superior photocatalytic performance could be attributed to the low electron–hole recombination, massive surface active sites and high charge mobility of tellurene.

6.2 Photocatalytic CO_2 reduction reaction and the N_2 reduction reaction

Photocatalytic reduction of CO_2 and N_2 provides a valuable path to effectively mitigate the greenhouse effect as well as produce useful chemical fuels or high-value-adding chemicals. Elemental 2D materials have been studied as high-performance photocatalysts for the CO_2RR and NRR. For example, the BP-based composite has demonstrated excellent performance as a photocatalyst in photocatalytic CO_2RR.[222] The LPE-derived BP could uniformly self-assemble with the cubic perovskite nanocrystal $CsPbBr_3$ to form a heterostructure photocatalyst (Fig. 10a). As illustrated in Fig. 10b and c, the hybrid photocatalyst possessed good cycling performance and enhanced performance with high conversion rates of CO_2 to CO and CH_4 at 44.7 and 10.7 μmol g^{-1} h^{-1}, compared with the pure $CsPbBr_3$ nanocrystals or BP nanosheets. The high performance is ascribed to the efficient charge separation at the $CsPbBr_3$/BP interface that significantly reduced the recombination of photoinduced electrons and holes. Also, the introduction of BP provided more active sites, which facilitated the charge transfer kinetics of CO_2 reduction. In another work, the hydroxyl group was utilized to modify monolayer BP to enhance the electrochemical ability for the CO_2RR.[223] Isopropanol solution was added as a solvent for ultrasonication to add hydroxy functional groups to BP to enhance its stability. The hydroxyl-modified BP showed stable photocatalysis to reduce CO_2 to CO under visible light, with an impressive CO production rate of 112.6 μmol h^{-1} g^{-1}.

Interestingly, the aforementioned Te NS-ACS composite could also serve as a photocatalyst for efficient photocatalytic CO_2RR producing 104.5 μmol of CO within two hours.[220] The

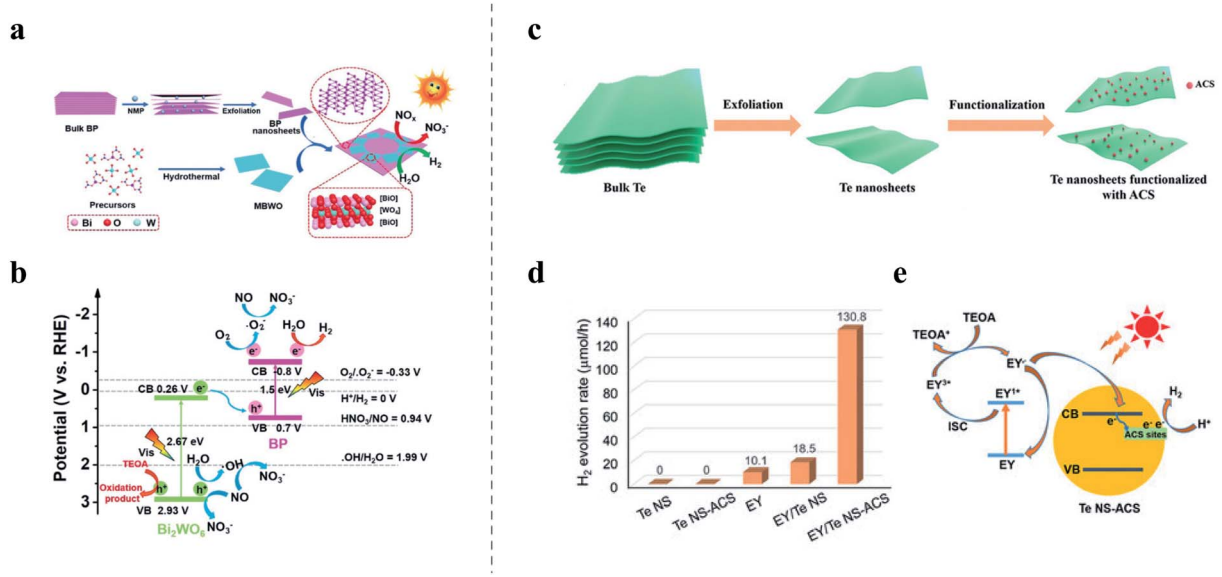

Fig. 9 (a and b) Photocatalytic NO removal based on the composite film of BP/monolayer Bi_2WO_6:[209] (a) schematic illustration of the synthesis of the BP/monolayer Bi_2WO_6 heterojunction; (b) mechanism of photocatalytic NO removal and water splitting based on the BP/monolayer Bi_2WO_6 heterojunction under visible-light irradiation, showing the various redox potentials *versus* RHE. (c–e) Photocatalytic H_2 evolution based on atomic cobalt species (ACS) functionalized tellurene nanosheets (Te NS-ACS):[210] (c) illustration of the synthesis of Te NS-ACS; (d) the photocatalytic H_2 evolution activities of pure tellurene nanosheets (Te NS) with and without ACS functionalization and Eosin Y (EY) as a light absorber under visible light; (e) mechanism of the photocatalytic H_2 evolution based on Te NS-ACS. (a and b) Reproduced with permission,[209] Wiley-VCH. (c–e) Reproduced with permission,[210] Wiley-VCH.

functionalization of ACS introduces numerous intermediate energy states, trapping photoinduced electrons, which further suppresses the recombination of photogenerated carriers and contributes to high photocatalytic performance.

Most recently, elemental 2D materials have also found their use in photocatalytic nitrogen fixation. For example, the 2D BP/CdS hybrid is reported as an efficient photocatalyst for the NRR,[224] showing a photocurrent density of 13.58 μA cm^{-2}, which is much higher than that of pristine CdS (6.79 μA cm^{-2}). H_2 production was negligible, which demonstrates the high selectivity of CdS/2D BP photocatalyst for N_2 reduction. The DFT calculations revealed that BP nanosheets could extract electrons from adjacent CdS, which suppresses photoinduced electron–hole recombination and promotes photocatalytic performance.

6.3 Photocatalytic applications in environmental fields

Elemental 2D materials also show potential as metal-free photocatalysts for photoinduced H_2O_2 production and water purification. A heterostructure photocatalyst based on the hybrid of BP and graphitic carbon nitride (g-C_3N_4) was reported recently.[225] The composite exhibited excellent photocatalytic performance for light-induced superoxide radical ($^{\bullet}O_2^-$) evolution and consequently showed an elevated ability in rhodamine B (RhB) degradation. The degradation rates of RhB after 15 min photoreaction for 10% BP/C_3N_4, C_3N_4, and BP nanosheets were 98%, 55%, and 2%, respectively. The enhanced performance of BP/g-C_3N_4 could be attributed to the visible light adsorption of BP and high charge separation efficiency at the heterojunction interface. Remarkably, the photocatalytic H_2O_2 generation rate of BP/g-C_3N_4 reached 3463 μmol h^{-1} g^{-1}, which was about 14.5 times higher than that of bulk g-C_3N_4.

7. Application in solar cells

Solar cells, which can turn unlimited solar energy into electric energy, have been developed and utilized practically since the 1970s. The most recent development in nanomaterials, especially 2D materials, provides enormous opportunities for high-performance solar cells beyond conventional bulk materials. Notably, some elemental 2D materials with high carrier mobility and tunable band gaps are considered to be promising candidates for solar cells.

Many theoretical studies have investigated the potential of elemental 2D materials in solar cells.[226] For example, Hu *et al.* constructed the heterostructure consisting of hydrogen atom or fluorine atom-modified phosphorene nanoflakes and studied its optoelectronic properties.[227] Based on calculation result, the heterojunction is predicted to exhibit a high energy conversion efficiency of 20%, making them suitable for high efficiency and low-cost solar cells. Additionally, tellurene possesses a suitable band gap, high carrier mobility and strong light absorption, which make it promising for solar cells.[228] By using first-principles density functional theory (DFT) calculations, Gao *et al.* demonstrated that the heterojunction constructed from halogen-modified zigzag tellurene possesses desirable type 2 band alignments, small band offsets and reduced band gaps for enhanced sunlight absorption, resulting in a high power-conversion efficiency (PCE) of 22.6% in heterojunction solar cells.

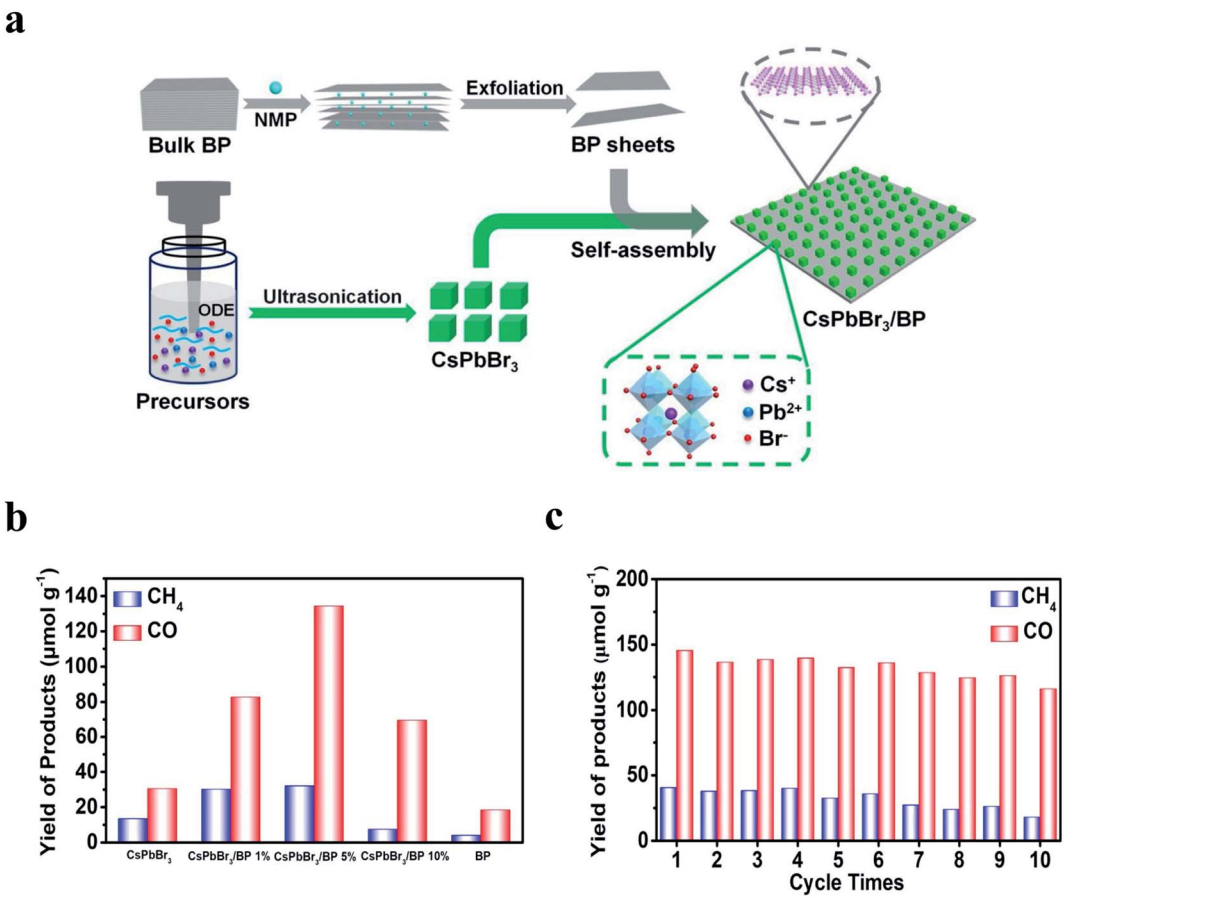

Fig. 10 Photocatalytic CO_2RR based on the heterostructure of the cubic perovskite nanocrystal ($CsPbBr_3$) assembled on BP ($CsPbBr_3$/BP):[212] (a) schematic illustration of the synthesis of $CsPbBr_3$/BP. (b) The production of CH_4 (blue) and CO (red) in ethyl acetate with 0.4 vol% H_2O solvents after 3 h based on $CsPbBr_3$/BP with different weight ratios of BP. (c) Cycle stability of photocatalytic CO_2 reduction under light irradiation based on $CsPbBr_3$/BP. Reproduced with permission,[212] Elsevier.

Experimental investigation of elemental 2D materials for solar cells has also been carried out recently. LPE-derived antimonene quantum dots were applied as effective photoactive materials in solid-state solar cells.[229] Antimonene has good optical absorption due to its approximately 1.5 eV band gap, which is close to ideal for a solar absorber, along with high light stability. The fabricated solar cells exhibited an encouraging PCE of 3.07% in the forward and reverse scan modes (without employing any interfacial optimization) and good stability with 90% of the initial PCE maintained after 1000 hours of operation. Besides, monolayer antimonene nanosheets are ideal for the hole extraction layer in planar inverted perovskite solar cells.[230] And it can effectively improve the PCE of perovskite solar cells from 17.58% to 20.05%, due to fast hole extraction and efficient hole transfer at the perovskite/hole transport layer interface.

The various applications of elemental 2D materials in energy fields are summarized in Table 2. From Table 2, one can see that though phosphorene, bismuthene and antimonene are well studied in the energy storage and conversation fields to date; research on materials such as gallinene and plumbene is still in its infancy stage. Furthermore, most of the research of moderately well-studied elemental 2D materials (arsenene, germanene, and stanene) heavily lean on battery applications, indicating extensive opportunities to explore other energy applications.

8. Summary and outlook

In the past decade, significant progress has been made in the theoretical and experimental exploration of elemental 2D materials, which immensely expand the scope of the ever-growing 2D materials family. Elemental 2D materials possess many unique properties, including large specific areas, abundant active sites, tunable band gaps and high carrier mobility, showing potential in various energy fields, including batteries, electrocatalysis and photocatalysis. The synthetic difficulties, along with the stability issues, have severely limited the practical applications of elemental 2D materials. While the continuous progress targeting the synthetic challenges has been summarized in previous sections, researchers have recently made great efforts to stabilize emerging elemental 2D materials to expand their applications scope and enhance the performance. For example, BP, as one of the most promising, has been modified in various ways to achieve commendable stability in batteries, electrocatalysis and photocatalysis.

Table 2 Summary of the performance of elemental 2D materials and other typical 2D materials in various energy fields[a]

			Emerging elemental 2D materials	Typical materials
Batteries (mA h^{-1} g^{-1})	LIB	*Th.*	B: 1860,[158] Si: 954,[160] Ge: 369,[160] Sn: 226,[160] As: 1609 (ref. 161)	Graphite: 372,[231] MoS_2: 334,[232] Ti_3C_2: 320 (ref. 233)
		Exp.	BP: 920@0.1 A g^{-1},[163] Sb: 584@0.5C (ref. 165)	MoS_2: 912@1C (ref. 234)
	SIB	*Th.*	As: 1073 (ref. 161)	MoS_2: 670 (ref. 235)
		Exp.	BP: 2440@0.05 A g^{-1},[169] Sb: 642@0.1C,[74] Bi: 381@0.2 mA cm^{-2},[45] I: 250@0.1 A g^{-1} (ref. 51)	Graphite: 284@20 mA g^{-1},[236] MXene: 267@0.1 A g^{-1},[237] MoS_2: from 190 to 85 after 100 cycle[238]
	Others		BP and borophene show potential as a good host of the cathode material for LSB.[171,173] Zn–Te battery exhibits a high capacity of 419 mA h^{-1} g^{-1}@0.05 A g^{-1} (ref. 174)	
Supercapacitor (F g^{-1})			BP: 478@1 A g^{-1},[177] Sb: 1578@14 A g^{-1} (ref. 180)	MoS_2: 100@1 mV s^{-1},[239] Ti_3C_2: 245@2 mV s^{-1} (ref. 240)
Electrocatalysis (mV *vs.* RHE)@10 mA cm^{-2}	HER		BP: 290 in 1 M KOH,[241] Sb: 153 in buffer[189]	2H-MoS_2: 208 in 0.5 M H_2SO_4,[242] 1T-MoS_2: 252 in 0.5 M H_2SO_4,[243] WSe_2: 245 in 0.5 M H_2SO_4 (ref. 244)
	OER		B: 240 (*Th.*),[190] BP: 430 in 1 M NaOH,[245] Sb: 1.56 V in 1 M KOH (ref. 186)	MoS_2: 450 in 0.5 M H_2SO_4,[246] Co_3O_4: 318 in 1 M NaOH (ref. 247)
	ORR		B: 470 (*Th.*)[190]	
	NRR		BP: faradaic efficiency of 5.0%@−0.7 V in 0.01 M HCl (ref. 192)	
	CO_2RR		Bi: faradaic efficiency >95%@−1.5 V (ref. 196)	
Photocatalysis (*Exp.*)			BP: H_2 evolution rate: 21 042 μmol h^{-1} g^{-1};[218] NO removal ratio: 67%;[218] CO_2RR: CO and CH_4 evolution rate of 44.7 and 10.7 μmol g^{-1} h^{-1};[222] NRR: NH_3 evolution rate of 57.64 μmol L^{-1} h^{-1} (ref. 224) Te: H_2 evolution rate: 130.8 μmol h^{-1};[220] CO_2RR: 104.5 μmol CO (2 h)[220]	MoS_2: H_2 evolution rate: 1472 μmol h^{-1} g^{-1},[248] 1T-MoS_2: H_2 evolution rate: 26 000 μmol h^{-1} g^{-1} (ref. 249)
Solar cell (power conversion efficiency)	*Th.*		Si: 29%,[226] Te: 22.6%,[228] BP: 20% (ref. 227)	Bulk GaAs: ∼30% (ref. 250)
	Exp.		Sb: 3.07% (ref. 229)	MoS_2: 5.23% (ref. 251)

[a] LIB is the Li-ion battery; SIB is the Na-ion battery; LSB is the Li–sulfur battery; HER is the hydrogen evolution reaction, OER is the oxygen evolution reaction; CO_2RR is the CO_2 reduction reaction, and NRR is the nitrogen reduction reaction. *Th.* is short for theory and *Exp*. is short for experiment.

Additionally, some elemental 2D materials in groups 15 and 16 (including antimonene, tellurene, arsenene, *etc.*) exhibit higher mobility than TMD and higher stability than BP, and are more likely to shine in practical applications in the near future.[252] For example, tellurene, which can be synthesized on a large scale *via* the facile hydrothermal method, demonstrates great potential in high-performance cathodes for Zn–Te batteries, as well as in other energy and electronic applications, such as solar cells, photodetectors and gas sensors.[93] In addition, restricted by the synthetic approaches, the applications of many emerging elemental 2D materials in groups 13 and 14 still require further investigation.

Although immerse advances have been made in the realization and practical application of elemental 2D materials, the rapidly expanding elemental 2D materials are still an emerging area that faces plenty of difficulties. Several critical issues and possible solutions are discussed below.

First of all, we recognize the incredible challenges in the synthesis of elemental 2D materials with high yield and sizeable lateral dimensions. In one respect, some elemental materials, such as silicene and borophene, are impossible to obtain *via* direct exfoliation of bulky sources due to the strong sp^3 hybridized bonds. Synthesis of these elemental 2D materials currently relies on MBE, which is not only demanding in terms of the equipment, reaction conditions and substrates, but is also impractical for large-scale applications. In the other respect, traditional widely applied exfoliation methods and other bottom-up methods are also limited by either the crystal quality or product lateral size. To this end, more efforts in developing novel synthetic methods towards high-quality and high-yield production of elemental 2D materials remain the priority in this growing field.

Second, significant knowledge gaps between the theoretical studies and experimental results still challenge the further development of elemental 2D materials for energy applications in terms of structures, properties, and operational mechanisms. First of all, although great progress has been achieved in expanding the elemental 2D material family experimentally, the synthesis of many previously predicted structures, such as aluminene (2D aluminum),[49] indiene (2D indium),[50] few-layer graphdiyne,[253] penta-graphene[64] and green phosphorene,[254] still necessitates more effort. Additionally, there are some crucial discrepancies about the band structures of elemental 2D

materials between the predicted and experiment results, such as black arsenene and tellurene. Moreover, despite the fact that abundant theoretical results have revealed a variety of potential energy applications for various elemental 2D materials, experimental realization calls for further attempts. For example, borophene is considered to be a promising electrode material for Li–S batteries. However, it has not been experimentally verified yet until now.

Third, the heterostructures of elemental 2D materials and other nanomaterials ranging from 2D materials to 0D nanoparticles could significantly expand the capability of elemental 2D materials. The heterostructure strategy could provide more new properties inaccessible to the individual components due to various synergistic effects. For example, the aforementioned Ru–S–Sb/antimonene[189] and $CsPbBr_3$/black[222] heterostructures have shown improved catalytic performance compared with the individual components. Specifically, 2D van der Waals heterojunctions (vdWHs) have invoked substantial interest due to their ability to tailor the electronic properties of 2D structures through interfacial coupling,[255] which could effectively optimize performance in energy applications. For example, the BP g-C_3N_4 2D/2D van der Waals heterostructure reduced photoinduced carrier recombination and exhibited enhanced photocatalysis performance compared to the pure BP nanosheets or g-C_3N_4 nanosheets.[256]

Fourth, the achievement in the synthetic effort of emerging elemental 2D materials calls for further exploration in novel energy applications beyond electrochemistry. The large surface area, tunable band structures and diverse interfacial properties could shine in alternative energy conversion technologies such as solar-thermal clean water production[219,220] or electrokinetic power generation.[221,222]

Last but not least, the development of novel characterization techniques could offer new perspectives in the investigation of emerging nanomaterials, including elemental 2D materials, which is especially beneficial for the mechanism study in energy applications. Recently, a variety of advanced characterization techniques have been incorporated in the investigation of energy storage and photo-/electro-catalysts, such as *in situ* Raman spectroscopy,[257,258] *in situ* XRD spectra,[259] cryogenic transmission electron microscopy,[260,261] *in situ* transmission electron microscopy,[262,263] and many more. Remarkably, the recently developed on-chip electrochemical approach[4,264,265] is particularly suitable for the electrochemical applications of 2D electrocatalysts with a limited size, yield and stability, as well as diverse crystal phases,[266,267] which could significantly expand the exploration of elemental 2D materials and their heterostructures in energy applications.

Conflicts of interest

There are no conflicts to declare.

Acknowledgements

Q. H. acknowledges the support from the Start-Up Grant (project no. 7200656 and 9610482) and Grants (project no. 7005468) from the City University of Hong Kong.

References

1 A. K. Geim and K. S. Novoselov, *Nat. Mater.*, 2007, **6**, 183–191.
2 C. Tan, X. Cao, X.-J. Wu, Q. He, J. Yang, X. Zhang, J. Chen, W. Zhao, S. Han, G.-H. Nam, M. Sindoro and H. Zhang, *Chem. Rev.*, 2017, **117**, 6225–6331.
3 K. Zhang, Y. Feng, F. Wang, Z. Yang and J. Wang, *J. Mater. Chem. C*, 2017, **5**, 11992–12022.
4 Y. He, Q. He, L. Wang, C. Zhu, P. Golani, A. D. Handoko, X. Yu, C. Gao, M. Ding, X. Wang, F. Liu, Q. Zeng, P. Yu, S. Guo, B. I. Yakobson, L. Wang, Z. W. Seh, Z. Zhang, M. Wu, Q. J. Wang, H. Zhang and Z. Liu, *Nat. Mater.*, 2019, **18**, 1098–1104.
5 A. J. Mannix, B. Kiraly, M. C. Hersam and N. P. Guisinger, *Nat. Rev. Chem.*, 2017, **1**, 0014.
6 W. Tao, N. Kong, X. Ji, Y. Zhang, A. Sharma, J. Ouyang, B. Qi, J. Wang, N. Xie, C. Kang, H. Zhang, O. C. Farokhzad and J. S. Kim, *Chem. Soc. Rev.*, 2019, **48**, 2891–2912.
7 N. R. Glavin, R. Rao, V. Varshney, E. Bianco, A. Apte, A. Roy, E. Ringe and P. M. Ajayan, *Adv. Mater.*, 2020, **32**, 1904302.
8 Z. Lin, C. Wang and Y. Chai, *Small*, 2020, **16**, 2003319.
9 Z. Meng, J. Zhuang, X. Xu, W. Hao, S. X. Dou and Y. Du, *Adv. Mater. Interfaces*, 2018, **5**, 1800749.
10 M. Qiu, Z. T. Sun, D. K. Sang, X. G. Han, H. Zhang and C. M. Niu, *Nanoscale*, 2017, **9**, 13384–13403.
11 Y. Xu, Z. Shi, X. Shi, K. Zhang and H. Zhang, *Nanoscale*, 2019, **11**, 14491–14527.
12 T. Wang, H. Wang, Z. Kou, W. Liang, X. Luo, F. Verpoort, Y.-J. Zeng and H. Zhang, *Adv. Funct. Mater.*, 2020, **30**, 2002885.
13 M. Z. Mohamad Nasir and M. Pumera, *TrAC, Trends Anal. Chem.*, 2019, **121**, 115696.
14 N. Antonatos, H. Ghodrati and Z. Sofer, *Appl. Mater. Today*, 2020, **18**, 100502.
15 A. J. Mannix, X.-F. Zhou, B. Kiraly, J. D. Wood, D. Alducin, B. D. Myers, X. Liu, B. L. Fisher, U. Santiago, J. R. Guest, M. J. Yacaman, A. Ponce, A. R. Oganov, M. C. Hersam and N. P. Guisinger, *Science*, 2015, **350**, 1513–1516.
16 B. Feng, L. Chen and K. Wu, in *2D Boron: Boraphene, Borophene, Boronene*, 2021, ch. 3, pp. 51–72, DOI: 10.1007/978-3-030-49999-0_3.
17 M.-L. Tao, Y.-B. Tu, K. Sun, Y.-L. Wang, Z.-B. Xie, L. Liu, M.-X. Shi and J.-Z. Wang, *2D Mater.*, 2018, **5**, 035009.
18 G. Tai, T. Hu, Y. Zhou, X. Wang, J. Kong, T. Zeng, Y. You and Q. Wang, *Angew. Chem., Int. Ed.*, 2015, **127**, 15693–15697.
19 S. Zhang, Z. Yan, Y. Li, Z. Chen and H. Zeng, *Angew. Chem., Int. Ed.*, 2015, **54**, 3112–3115.
20 B. Feng, J. Zhang, Q. Zhong, W. Li, S. Li, H. Li, P. Cheng, S. Meng, L. Chen and K. Wu, *Nat. Chem.*, 2016, **8**, 563–568.
21 S. Xu, Y. Zhao, J. Liao, X. Yang and H. Xu, *Nano Res.*, 2016, **9**, 2616–2622.
22 Q. Zhong, L. Kong, J. Gou, W. Li, S. Sheng, S. Yang, P. Cheng, H. Li, K. Wu and L. Chen, *Phys. Rev. Mater.*, 2017, **1**, 021001.

23 Q. Zhong, J. Zhang, P. Cheng, B. Feng, W. Li, S. Sheng, H. Li, S. Meng, L. Chen and K. Wu, *J. Phys.: Condens. Matter*, 2017, **29**, 095002.
24 G. P. Campbell, A. J. Mannix, J. D. Emery, T.-L. Lee, N. P. Guisinger, M. C. Hersam and M. J. Bedzyk, *Nano Lett.*, 2018, **18**, 2816–2821.
25 X. Ji, N. Kong, J. Wang, W. Li, Y. Xiao, S. T. Gan, Y. Zhang, Y. Li, X. Song and Q. Xiong, *Adv. Mater.*, 2018, **30**, 1803031.
26 W. Li, L. Kong, C. Chen, J. Gou, S. Sheng, W. Zhang, H. Li, L. Chen, P. Cheng and K. Wu, *Sci. Bull.*, 2018, **63**, 282–286.
27 B. Kiraly, X. Liu, L. Wang, Z. Zhang, A. J. Mannix, B. L. Fisher, B. I. Yakobson, M. C. Hersam and N. P. Guisinger, *ACS Nano*, 2019, **13**, 3816–3822.
28 N. A. Vinogradov, A. Lyalin, T. Taketsugu, A. S. Vinogradov and A. Preobrajenski, *ACS Nano*, 2019, **13**, 14511–14518.
29 R. Wu, I. K. Drozdov, S. Eltinge, P. Zahl, S. Ismail-Beigi, I. Božović and A. Gozar, *Nat. Nanotechnol.*, 2019, **14**, 44–49.
30 R. Wu, A. Gozar and I. Božović, *npj Quantum Mater.*, 2019, **4**, 40.
31 H. Liu, J. Gao and J. Zhao, *J. Phys. Chem. C*, 2013, **117**, 10353–10359.
32 L. Zhang, H. Huang, B. Zhang, M. Gu, D. Zhao, X. Zhao, L. Li, J. Zhou, K. Wu, Y. Cheng and J. Zhang, *Angew. Chem., Int. Ed.*, 2020, **59**, 1074–1080.
33 W. Zhang, H. Enriquez, Y. Tong, A. Bendounan, A. Kara, A. P. Seitsonen, A. J. Mayne, G. Dujardin and H. Oughaddou, *Small*, 2018, **14**, 1804066.
34 A. E. Del Rio Castillo, V. Pellegrini, H. Sun, J. Buha, D. A. Dinh, E. Lago, A. Ansaldo, A. Capasso, L. Manna and F. Bonaccorso, *Chem. Mater.*, 2018, **30**, 506–516.
35 R. Feng, W. Lei, G. Liu and M. Liu, *Adv. Mater.*, 2018, **30**, 1804770.
36 W. Huang, C. Li, L. Gao, Y. Zhang, Y. Wang, Z. N. Huang, T. Chen, L. Hu and H. Zhang, *J. Mater. Chem. C*, 2020, **8**, 1172–1197.
37 M. J. Cherukara, B. Narayanan, H. Chan and S. K. Sankaranarayanan, *Nanoscale*, 2017, **9**, 10186–10192.
38 J. Yuhara, H. Shimazu, K. Ito, A. Ohta, M. Araidai, M. Kurosawa, M. Nakatake and G. Le Lay, *ACS Nano*, 2018, **12**, 11632–11637.
39 J. Yuhara, Y. Fujii, K. Nishino, N. Isobe, M. Nakatake, L. Xian, A. Rubio and G. Le Lay, *2D Mater.*, 2018, **5**, 025002.
40 J. Yuhara, B. He, N. Matsunami, M. Nakatake and G. Le Lay, *Adv. Mater.*, 2019, **31**, 1901017.
41 Z. Wang, X.-F. Zhou, X. Zhang, Q. Zhu, H. Dong, M. Zhao and A. R. Oganov, *Nano Lett.*, 2015, **15**, 6182–6186.
42 S. Zhang, J. Zhou, Q. Wang, X. Chen, Y. Kawazoe and P. Jena, *Proc. Natl. Acad. Sci. U. S. A.*, 2015, **112**, 2372–2377.
43 Y. Zhang, L. Wang, H. Xu, J. Cao, D. Chen and W. Han, *Adv. Funct. Mater.*, 2020, **30**, 1909372.
44 X. Wang, J. He, B. Zhou, Y. Zhang, J. Wu, R. Hu, L. Liu, J. Song and J. Qu, *Angew. Chem., Int. Ed.*, 2018, **130**, 8804–8809.
45 J. Zhou, J. Chen, M. Chen, J. Wang, X. Liu, B. Wei, Z. Wang, J. Li, L. Gu, Q. Zhang, H. Wang and L. Guo, *Adv. Mater.*, 2019, **31**, 1807874.
46 S. M. Beladi-Mousavi, A. M. Pourrahimi, Z. Sofer and M. Pumera, *Adv. Funct. Mater.*, 2019, **29**, 1807004.
47 J. Chen, Y. Dai, Y. Ma, X. Dai, W. Ho and M. Xie, *Nanoscale*, 2017, **9**, 15945–15948.
48 J. Qin, G. Qiu, J. Jian, H. Zhou, L. Yang, A. Charnas, D. Y. Zemlyanov, C.-Y. Xu, X. Xu, W. Wu, H. Wang and P. D. Ye, *ACS Nano*, 2017, **11**, 10222–10229.
49 J. Yuan, N. Yu, K. Xue and X. Miao, *Appl. Surf. Sci.*, 2017, **409**, 85–90.
50 D. Singh, S. K. Gupta, I. Lukačević and Y. Sonvane, *RSC Adv.*, 2016, **6**, 8006–8014.
51 M. Qian, Z. Xu, Z. Wang, B. Wei, H. Wang, S. Hu, L.-M. Liu and L. Guo, *Adv. Mater.*, 2020, **32**, 2004835.
52 V. Kochat, A. Samanta, Y. Zhang, S. Bhowmick, P. Manimunda, S. A. S. Asif, A. S. Stender, R. Vajtai, A. K. Singh, C. S. Tiwary and P. M. Ajayan, *Sci. Adv.*, 2018, **4**, e1701373.
53 A. Molle, J. Goldberger, M. Houssa, Y. Xu, S.-C. Zhang and D. J. N. m. Akinwande, *Nat. Mater.*, 2017, **16**, 163–169.
54 J. Deng, B. Xia, X. Ma, H. Chen, H. Shan, X. Zhai, B. Li, A. Zhao, Y. Xu and W. Duan, *Nat. Mater.*, 2018, **17**, 1081–1086.
55 S. Balendhran, S. Walia, H. Nili, S. Sriram and M. Bhaskaran, *Small*, 2015, **11**, 640–652.
56 P. Vogt, P. De Padova, C. Quaresima, J. Avila, E. Frantzeskakis, M. C. Asensio, A. Resta, B. Ealet and G. Le Lay, *Phys. Rev. Lett.*, 2012, **108**, 155501.
57 P. Rivero, J.-A. Yan, V. M. García-Suárez, J. Ferrer and S. Barraza-Lopez, *Phys. Rev. B*, 2014, **90**, 241408.
58 F. Matusalem, M. Marques, L. K. Teles and F. Bechstedt, *Phys. Rev. B*, 2015, **92**, 045436.
59 D. Wang, L. Chen, X. Wang, G. Cui and P. Zhang, *Phys. Chem. Chem. Phys.*, 2015, **17**, 26979–26987.
60 J. C. Garcia, D. B. De Lima, L. V. Assali and J. F. Justo, *Phys. Chem. Chem. Phys.*, 2011, **115**, 13242–13246.
61 X. Fan, J. Li and G. Chen, *RSC Adv.*, 2017, **7**, 17417–17426.
62 G. Long, Y. Zhou, M. Jin, B. Kan, Y. Zhao, A. Gray-Weale, D.-e. Jiang, Y. Chen and Q. Zhang, *Carbon*, 2015, **95**, 1033–1038.
63 J.-W. Jiang, J. Leng, J. Li, Z. Guo, T. Chang, X. Guo and T. Zhang, *Carbon*, 2017, **118**, 370–375.
64 Y. Aierken, O. Leenaerts and F. M. Peeters, *Phys. Rev. B*, 2016, **94**, 155410.
65 D. Wu, S. Wang, J. Yuan, B. Yang and H. Chen, *Phys. Chem. Chem. Phys.*, 2017, **19**, 11771–11777.
66 X. Wang, A. M. Jones, K. L. Seyler, V. Tran, Y. Jia, H. Zhao, H. Wang, L. Yang, X. Xu and F. Xia, *Nat. Nanotechnol.*, 2015, **10**, 517–521.
67 C. Zhang, X. Peng, Z. Guo, C. Cai, Z. Chen, D. Wexler, S. Li and H. Liu, *Carbon*, 2012, **50**, 1897–1903.
68 J. Pang, A. Bachmatiuk, Y. Yin, B. Trzebicka, L. Zhao, L. Fu, R. G. Mendes, T. Gemming, Z. Liu and M. H. Rummeli, *Adv. Energy Mater.*, 2018, **8**, 1702093.
69 Q. He, Y. Liu, C. Tan, W. Zhai, G.-h. Nam and H. Zhang, *ACS Nano*, 2019, **13**, 12294–12300.
70 J. Qiao, X. Kong, Z.-X. Hu, F. Yang and W. Ji, *Nat. Commun.*, 2014, **5**, 4475.

71 X. Zhu, T. Zhang, Z. Sun, H. Chen, J. Guan, X. Chen, H. Ji, P. Du and S. Yang, *Adv. Mater.*, 2017, **29**, 1605776.
72 A. Favron, E. Gaufrès, F. Fossard, A.-L. Phaneuf-L'Heureux, N. Y. W. Tang, P. L. Lévesque, A. Loiseau, R. Leonelli, S. Francoeur and R. Martel, *Nat. Mater.*, 2015, **14**, 826–832.
73 G. Wang, W. J. Slough, R. Pandey and S. P. Karna, *2D Mater.*, 2016, **3**, 025011.
74 W. Tian, S. Zhang, C. Huo, D. Zhu, Q. Li, L. Wang, X. Ren, L. Xie, S. Guo, P. K. Chu, H. Zeng and K. Huo, *ACS Nano*, 2018, **12**, 1887–1893.
75 X. Wu, Y. Shao, H. Liu, Z. Feng, Y.-L. Wang, J.-T. Sun, C. Liu, J.-O. Wang, Z.-L. Liu, S.-Y. Zhu, Y.-Q. Wang, S.-X. Du, Y.-G. Shi, K. Ibrahim and H.-J. Gao, *Adv. Mater.*, 2017, **29**, 1605407.
76 Q. Wu and Y. J. Song, *Chem. Commun.*, 2018, **54**, 9671–9674.
77 S. Zhang, M. Xie, F. Li, Z. Yan, Y. Li, E. Kan, W. Liu, Z. Chen and H. Zeng, *Angew. Chem., Int. Ed.*, 2016, **128**, 1698–1701.
78 T. Chai, X. Li, T. Feng, P. Guo, Y. Song, Y. Chen and H. Zhang, *Nanoscale*, 2018, **10**, 17617–17622.
79 E. S. Walker, S. R. Na, D. Jung, S. D. March, J.-S. Kim, T. Trivedi, W. Li, L. Tao, M. L. Lee, K. M. Liechti, D. Akinwande and S. R. Bank, *Nano Lett.*, 2016, **16**, 6931–6938.
80 M. Zhong, Q. Xia, L. Pan, Y. Liu, Y. Chen, H.-X. Deng, J. Li and Z. Wei, *Adv. Funct. Mater.*, 2018, **28**, 1802581.
81 C. Kamal and M. Ezawa, *Phys. Rev. B*, 2015, **91**, 085423.
82 P. Vishnoi, M. Mazumder, S. K. Pati and C. N. R. Rao, *New J. Chem.*, 2018, **42**, 14091–14095.
83 Y.-p. Wang, C.-w. Zhang, W.-x. Ji, R.-w. Zhang, P. Li, P.-j. Wang, M.-j. Ren, X.-l. Chen and M. Yuan, *J. Phys. D: Appl. Phys.*, 2016, **49**, 055305.
84 Y. Hu, Z.-H. Qi, J. Lu, R. Chen, M. Zou, T. Chen, W. Zhang, Y. Wang, X. Xue, J. Ma and Z. Jin, *Chem. Mater.*, 2019, **31**, 4524–4535.
85 J. Carrete, L. J. Gallego and N. Mingo, *J. Phys. Chem. Lett.*, 2017, **8**, 1375–1380.
86 Y. Chen, C. Chen, R. Kealhofer, H. Liu, Z. Yuan, L. Jiang, J. Suh, J. Park, C. Ko, H. S. Choe, J. Avila, M. Zhong, Z. Wei, J. Li, S. Li, H. Gao, Y. Liu, J. Analytis, Q. Xia, M. C. Asensio and J. Wu, *Adv. Mater.*, 2018, **30**, 1800754.
87 D. Guo, B. Shao, C. Li and Y. Ma, *Superlattices Microstruct.*, 2016, **100**, 324–334.
88 B. Peng, H. Zhang, H. Shao, K. Xu, G. Ni, J. Li, H. Zhu and C. M. Soukoulis, *J. Mater. Chem. A*, 2018, **6**, 2018–2033.
89 Y. Wang, G. Qiu, R. Wang, S. Huang, Q. Wang, Y. Liu, Y. Du, W. A. Goddard, M. J. Kim, X. Xu, P. D. Ye and W. Wu, *Nat. Electron.*, 2018, **1**, 228–236.
90 X. Huang, J. Guan, Z. Lin, B. Liu, S. Xing, W. Wang and J. Guo, *Nano Lett.*, 2017, **17**, 4619–4623.
91 J. Qiao, Y. Pan, F. Yang, C. Wang, Y. Chai and W. Ji, *Sci. Bull.*, 2018, **63**, 159–168.
92 C. Shen, Y. Liu, J. Wu, C. Xu, D. Cui, Z. Li, Q. Liu, Y. Li, Y. Wang, X. Cao, H. Kumazoe, F. Shimojo, A. Krishnamoorthy, R. K. Kalia, A. Nakano, P. D. Vashishta, M. R. Amer, A. N. Abbas, H. Wang, W. Wu and C. Zhou, *ACS Nano*, 2020, **14**, 303–310.
93 W. Wu, G. Qiu, Y. Wang, R. Wang and P. Ye, *Chem. Soc. Rev.*, 2018, **47**, 7203–7212.
94 J. C. Meyer, A. K. Geim, M. I. Katsnelson, K. S. Novoselov, T. J. Booth and S. Roth, *Nature*, 2007, **446**, 60–63.
95 L. Li, Y. Yu, G. J. Ye, Q. Ge, X. Ou, H. Wu, D. Feng, X. H. Chen and Y. Zhang, *Nat. Nanotechnol.*, 2014, **9**, 372–377.
96 P. Ares, F. Aguilar-Galindo, D. Rodríguez-San-Miguel, D. A. Aldave, S. Díaz-Tendero, M. Alcamí, F. Martín, J. Gómez-Herrero and F. Zamora, *Adv. Mater.*, 2016, **28**, 6332–6336.
97 C. Sabater, D. Gosálbez-Martínez, J. Fernández-Rossier, J. G. Rodrigo, C. Untiedt and J. J. Palacios, *Phys. Rev. Lett.*, 2013, **110**, 176802.
98 Y. Huang, E. Sutter, N. N. Shi, J. Zheng, T. Yang, D. Englund, H.-J. Gao and P. Sutter, *ACS Nano*, 2015, **9**, 10612–10620.
99 L. Guan, B. Xing, X. Niu, D. Wang, Y. Yu, S. Zhang, X. Yan, Y. Wang and J. Sha, *Chem. Commun.*, 2018, **54**, 595–598.
100 P. Yasaei, B. Kumar, T. Foroozan, C. Wang, M. Asadi, D. Tuschel, J. E. Indacochea, R. F. Klie and A. Salehi-Khojin, *Adv. Mater.*, 2015, **27**, 1887–1892.
101 W. Zheng, J. Lee, Z.-W. Gao, Y. Li, S. Lin, S. P. Lau and L. Y. S. Lee, *Adv. Energy Mater.*, 2020, **10**, 1903490.
102 J. Kang, J. D. Wood, S. A. Wells, J.-H. Lee, X. Liu, K.-S. Chen and M. C. Hersam, *ACS Nano*, 2015, **9**, 3596–3604.
103 A. O'Neill, U. Khan, P. N. Nirmalraj, J. Boland and J. N. Coleman, *J. Phys. Chem. C*, 2011, **115**, 5422–5428.
104 C. Gibaja, M. Assebban, I. Torres, M. Fickert, R. Sanchis-Gual, I. Brotons, W. S. Paz, J. J. Palacios, E. G. Michel, G. Abellán and F. Zamora, *J. Mater. Chem. A*, 2019, **7**, 22475–22486.
105 F. Liu, C. Wang, X. Sui, M. A. Riaz, M. Xu, L. Wei and Y. Chen, *Carbon Energy*, 2019, **1**, 173–199.
106 N. Liu, P. Kim, J. H. Kim, J. H. Ye, S. Kim and C. J. Lee, *ACS Nano*, 2014, **8**, 6902–6910.
107 C. Shen, T. Cheng, C. Liu, L. Huang, M. Cao, G. Song, D. Wang, B. Lu, J. Wang, C. Qin, X. Huang, P. Peng, X. Li and Y. Wu, *J. Mater. Chem. A*, 2020, **8**, 453–460.
108 J. Li, P. Song, J. Zhao, K. Vaklinova, X. Zhao, Z. Li, Z. Qiu, Z. Wang, L. Lin, M. Zhao, T. S. Herng, Y. Zuo, W. Jonhson, W. Yu, X. Hai, P. Lyu, H. Xu, H. Yang, C. Chen, S. J. Pennycook, J. Ding, J. Teng, A. H. Castro Neto, K. S. Novoselov and J. Lu, *Nat. Mater.*, 2021, **20**, 181–187.
109 C. Wang, Q. He, U. Halim, Y. Liu, E. Zhu, Z. Lin, H. Xiao, X. Duan, Z. Feng, R. Cheng, N. O. Weiss, G. Ye, Y.-C. Huang, H. Wu, H.-C. Cheng, I. Shakir, L. Liao, X. Chen, W. A. Goddard III, Y. Huang and X. Duan, *Nature*, 2018, **555**, 231–236.
110 A. Ambrosi, Z. Sofer and M. Pumera, *Angew. Chem., Int. Ed.*, 2017, **56**, 10443–10445.
111 M. B. Erande, S. R. Suryawanshi, M. A. More and D. J. Late, *Eur. J. Inorg. Chem.*, 2015, **2015**, 3102–3107.
112 Z. Huang, H. Hou, Y. Zhang, C. Wang, X. Qiu and X. Ji, *Adv. Mater.*, 2017, **29**, 1702372.

113 Z. Zeng, Z. Yin, X. Huang, H. Li, Q. He, G. Lu, F. Boey and H. Zhang, *Angew. Chem., Int. Ed.*, 2011, **123**, 11289–11293.
114 X. Tang, L. Hu, T. Fan, L. Zhang, L. Zhu, H. Li, H. Liu, J. Liang, K. Wang, Z. Li, S. Ruan, Y. Zhang, D. Fan, W. Chen, Y.-J. Zeng and H. Zhang, *Adv. Funct. Mater.*, 2019, **29**, 1808746.
115 Y. Yang, S. Leng and W. Shi, *Electrochem. Commun.*, 2021, **126**, 107025.
116 A. Lherbier, A. R. Botello-Méndez and J.-C. Charlier, *2D Mater.*, 2016, **3**, 045006.
117 T. Niu, W. Zhou, D. Zhou, X. Hu, S. Zhang, K. Zhang, M. Zhou, H. Fuchs and H. Zeng, *Adv. Mater.*, 2019, **31**, 1902606.
118 T. Paulauskas, F. G. Sen, C. Sun, P. Longo, Y. Zhang, S. W. Hla, M. K. Y. Chan, M. J. Kim and R. F. Klie, *Nanoscale*, 2019, **11**, 14698–14706.
119 Z. Y. Meng, T. C. Lang, S. Wessel, F. F. Assaad and A. Muramatsu, *Nature*, 2010, **464**, 847–851.
120 A. M. Attaran, S. Abdol-Manafi, M. Javanbakht and M. Enhessari, *J. Nanostruct. Chem.*, 2016, **6**, 121–128.
121 K. Kawahara, T. Shirasawa, R. Arafune, C.-L. Lin, T. Takahashi, M. Kawai and N. J. S. s. Takagi, *Surf. Sci.*, 2014, **623**, 25–28.
122 N. Takagi, C.-L. Lin, K. Kawahara, E. Minamitani, N. Tsukahara, M. Kawai and R. J. P. i. S. S. Arafune, *Appl. Surf. Sci.*, 2015, **90**, 1–20.
123 B. Feng, Z. Ding, S. Meng, Y. Yao, X. He, P. Cheng, L. Chen and K. Wu, *Nano Lett.*, 2012, **12**, 3507–3511.
124 P. De Padova, C. Quaresima, C. Ottaviani, P. M. Sheverdyaeva, P. Moras, C. Carbone, D. Topwal, B. Olivieri, A. Kara and H. J. A. P. L. Oughaddou, *Appl. Phys. Lett.*, 2010, **96**, 261905.
125 D. Chiappe, E. Scalise, E. Cinquanta, C. Grazianetti, B. van den Broek, M. Fanciulli, M. Houssa and A. Molle, *Adv. Mater.*, 2014, **26**, 2096–2101.
126 A. Fleurence, R. Friedlein, T. Ozaki, H. Kawai, Y. Wang and Y. Yamada-Takamura, *Phys. Rev. Lett.*, 2012, **108**, 245501.
127 L. Meng, Y. Wang, L. Zhang, S. Du, R. Wu, L. Li, Y. Zhang, G. Li, H. Zhou and W. A. Hofer, *Nano Lett.*, 2013, **13**, 685–690.
128 H. Enriquez, A. Mayne, A. Kara, S. Vizzini, S. Roth, B. Lalmi, A. P. Seitsonen, B. Aufray, T. Greber, R. Belkhou, G. Dujardin and H. Oughaddou, *Appl. Phys. Lett.*, 2012, **101**, 021605.
129 V. A. Lubarda, *Mech. Mater.*, 2003, **35**, 53–68.
130 K. T. Butler, P. E. Vullum, A. M. Muggerud, E. Cabrera and J. H. Harding, *Phys. Rev. B*, 2011, **83**, 235307.
131 M. Houssa, G. Pourtois, V. V. Afanas'ev and A. Stesmans, *Appl. Phys. Lett.*, 2010, **97**, 112106.
132 M. Houssa, G. Pourtois, M. M. Heyns, V. V. Afanas'ev and A. Stesmans, *J. Electrochem. Soc.*, 2011, **158**, H107.
133 E. Scalise, M. Houssa, E. Cinquanta, C. Grazianetti, B. van den Broek, G. Pourtois, A. Stesmans, M. Fanciulli and A. Molle, *2D Mater.*, 2014, **1**, 011010.
134 S. Kokott, P. Pflugradt, L. Matthes and F. Bechstedt, *J. Phys.: Condens. Matter*, 2014, **26**, 185002.
135 Y. Ding and Y. Wang, *Appl. Phys. Lett.*, 2013, **103**, 043114.
136 M. E. Dávila, L. Xian, S. Cahangirov, A. Rubio and G. Le Lay, *New J. Phys.*, 2014, **16**, 095002.
137 M. Derivaz, D. Dentel, R. Stephan, M.-C. Hanf, A. Mehdaoui, P. Sonnet and C. Pirri, *Nano Lett.*, 2015, **15**, 2510–2516.
138 L. Li, S.-z. Lu, J. Pan, Z. Qin, Y.-q. Wang, Y. Wang, G.-y. Cao, S. Du and H.-J. Gao, *Adv. Mater.*, 2014, **26**, 4820–4824.
139 A. Acun, L. Zhang, P. Bampoulis, M. Farmanbar, A. van Houselt, A. N. Rudenko, M. Lingenfelder, G. Brocks, B. Poelsema, M. I. Katsnelson and H. J. W. Zandvliet, *J. Phys.: Condens. Matter*, 2015, **27**, 443002.
140 Z. Qin, J. Pan, S. Lu, Y. Shao, Y. Wang, S. Du, H.-J. Gao and G. Cao, *Adv. Mater.*, 2017, **29**, 1606046.
141 F.-f. Zhu, W.-j. Chen, Y. Xu, C.-l. Gao, D.-d. Guan, C.-h. Liu, D. Qian, S.-C. Zhang and J.-f. Jia, *Nat. Mater.*, 2015, **14**, 1020–1025.
142 J. Gou, L. Kong, H. Li, Q. Zhong, W. Li, P. Cheng, L. Chen and K. Wu, *Phys. Rev. Mater.*, 2017, **1**, 054004.
143 A. T. Hoang, K. Qu, X. Chen and J.-H. Ahn, *Nanoscale*, 2021, **13**, 615–633.
144 M. Huang, B. Deng, F. Dong, L. Zhang, Z. Zhang and P. Chen, *Small Methods*, 2021, **5**, 2001213.
145 C. Li, Y. Wu, B. Deng, Y. Xie, Q. Guo, S. Yuan, X. Chen, M. Bhuiyan, Z. Wu, K. Watanabe, T. Taniguchi, H. Wang, J. J. Cha, M. Snure, Y. Fei and F. Xia, *Adv. Mater.*, 2018, **30**, 1703748.
146 H. Xu, X. Han, Z. Li, W. Liu, X. Li, J. Wu, Z. Guo and H. Liu, *Adv. Mater. Interfaces*, 2018, **5**, 1801048.
147 X. Zhang, J. Jiang, A. A. Suleiman, B. Jin, X. Hu, X. Zhou and T. Zhai, *Adv. Funct. Mater.*, 2019, **29**, 1906585.
148 G. Yang and S.-J. Park, *Materials*, 2019, **12**, 1177.
149 M. Amani, C. Tan, G. Zhang, C. Zhao, J. Bullock, X. Song, H. Kim, V. R. Shrestha, Y. Gao and K. Crozier, *ACS Nano*, 2018, **12**, 7253–7263.
150 L. Peng, S. Ye, J. Song and J. Qu, *Angew. Chem., Int. Ed.*, 2019, **58**, 9891–9896.
151 F. Yang, A. O. Elnabawy, R. Schimmenti, P. Song, J. Wang, Z. Peng, S. Yao, R. Deng, S. Song, Y. Lin, M. Mavrikakis and W. Xu, *Nat. Commun.*, 2020, **11**, 1088.
152 Y. Wang, S. Yao, P. Liao, S. Jin, Q. Wang, M. J. Kim, G. J. Cheng and W. Wu, *Adv. Mater.*, 2020, **32**, 2002342.
153 H. Xu, S. Yang and B. Li, *J. Mater. Chem. A*, 2020, **8**, 149–157.
154 M. A. Ledina, N. Bui, X. Liang, Y. G. Kim, J. Jung, B. Perdue, C. Tsang, J. Drnec, F. Carlà, M. P. Soriaga, T. J. Reber and J. L. Stickney, *J. Electrochem. Soc.*, 2017, **164**, D469–D477.
155 Z.-Q. Shi, H. Li, Q.-Q. Yuan, Y.-H. Song, Y.-Y. Lv, W. Shi, Z.-Y. Jia, L. Gao, Y.-B. Chen, W. Zhu and S.-C. Li, *Adv. Mater.*, 2019, **31**, 1806130.
156 S. Khatun, A. Banerjee and A. J. Pal, *Nanoscale*, 2019, **11**, 3591–3598.
157 W. Li, Y. Yang, G. Zhang and Y.-W. Zhang, *Nano Lett.*, 2015, **15**, 1691–1697.
158 H. R. Jiang, Z. Lu, M. C. Wu, F. Ciucci and T. S. Zhao, *Nano Energy*, 2016, **23**, 97–104.
159 Y. Huang, C. Zhu, S. Zhang, X. Hu, K. Zhang, W. Zhou, S. Guo, F. Xu and H. Zeng, *Nano Lett.*, 2019, **19**, 1118–1123.

160 B. Mortazavi, A. Dianat, G. Cuniberti and T. Rabczuk, *Electrochim. Acta*, 2016, **213**, 865–870.
161 H. Benzidi, M. Lakhal, M. Garara, M. Abdellaoui, A. Benyoussef, A. El kenz and O. Mounkachi, *Phys. Chem. Chem. Phys.*, 2019, **21**, 19951–19962.
162 L.-Q. Sun, M.-J. Li, K. Sun, S.-H. Yu, R.-S. Wang and H.-M. Xie, *J. Phys. Chem. C*, 2012, **116**, 14772–14779.
163 J. Sun, H.-W. Lee, M. Pasta, H. Yuan, G. Zheng, Y. Sun, Y. Li and Y. Cui, *Nat. Nanotechnol.*, 2015, **10**, 980–985.
164 Z. Zhang, S. N. Shirodkar, Y. Yang and B. I. Yakobson, *Angew. Chem., Int. Ed.*, 2017, **129**, 15623–15628.
165 Y. Gao, W. Tian, C. Huo, K. Zhang, S. Guo, S. Zhang, X. Song, L. Jiang, K. Huo and H. Zeng, *J. Mater. Chem. A*, 2019, **7**, 3238–3243.
166 M. I. Khan, G. Nadeem, A. Majid and M. Shakil, *Mater. Sci. Eng., B*, 2021, **266**, 115061.
167 Y. Dong, H. Shi and Z.-S. Wu, *Adv. Funct. Mater.*, 2020, **30**, 2000706.
168 H. Liu, K. Hu, D. Yan, R. Chen, Y. Zou, H. Liu and S. Wang, *Adv. Mater.*, 2018, **30**, 1800295.
169 L. Chen, G. Zhou, Z. Liu, X. Ma, J. Chen, Z. Zhang, X. Ma, F. Li, H.-M. Cheng and W. Ren, *Adv. Mater.*, 2016, **28**, 510–517.
170 P. G. Bruce, S. A. Freunberger, L. J. Hardwick and J.-M. Tarascon, *Nat. Mater.*, 2012, **11**, 19–29.
171 J. Sun, Y. Sun, M. Pasta, G. Zhou, Y. Li, W. Liu, F. Xiong and Y. Cui, *Adv. Mater.*, 2016, **28**, 9797–9803.
172 F. Li and J. Zhao, *ACS Appl. Mater. Interfaces*, 2017, **9**, 42836–42844.
173 H. R. Jiang, W. Shyy, M. Liu, Y. X. Ren and T. S. Zhao, *J. Mater. Chem. A*, 2018, **6**, 2107–2114.
174 Z. Chen, Q. Yang, F. Mo, N. Li, G. Liang, X. Li, Z. Huang, D. Wang, W. Huang, J. Fan and C. Zhi, *Adv. Mater.*, 2020, **32**, 2001469.
175 W. Raza, F. Ali, N. Raza, Y. Luo, K.-H. Kim, J. Yang, S. Kumar, A. Mehmood and E. E. Kwon, *Nano Energy*, 2018, **52**, 441–473.
176 S. Luo, J. Zhao, J. Zou, Z. He, C. Xu, F. Liu, Y. Huang, L. Dong, L. Wang and H. Zhang, *ACS Appl. Mater. Interfaces*, 2018, **10**, 3538–3548.
177 P. Nakhanivej, X. Yu, S. K. Park, S. Kim, J.-Y. Hong, H. J. Kim, W. Lee, J. Y. Hwang, J. E. Yang, C. Wolverton, J. Kong, M. Chhowalla and H. S. Park, *Nat. Mater.*, 2019, **18**, 156–162.
178 M. Ghidiu, M. R. Lukatskaya, M.-Q. Zhao, Y. Gogotsi and M. W. Barsoum, *Nature*, 2014, **516**, 78–81.
179 J. Yu, J. Zhou, P. Yao, H. Xie, M. Zhang, M. Ji, H. Liu, Q. Liu, C. Zhu and J. Xu, *Adv. Energy Mater.*, 2019, **9**, 1902462.
180 E. Martínez-Periñán, M. P. Down, C. Gibaja, E. Lorenzo, F. Zamora and C. E. Banks, *Adv. Energy Mater.*, 2018, **8**, 1702606.
181 M. Mohamed Ismail, J. Vigneshwaran, S. Arunbalaji, D. Mani, M. Arivanandhan, S. P. Jose and R. Jayavel, *Dalton Trans.*, 2020, **49**, 13717–13725.
182 V. K. Mariappan, K. Krishnamoorthy, P. Pazhamalai, S. Natarajan, S. Sahoo, S. S. Nardekar and S.-J. Kim, *Nano Energy*, 2020, **77**, 105248.
183 S. Singal, A. Joshi, G. Singh and R. K. Sharma, *J. Power Sources*, 2020, **475**, 228669.
184 S. H. Mir, S. Chakraborty, P. C. Jha, J. Wärnå, H. Soni, P. K. Jha and R. Ahuja, *Appl. Phys. Lett.*, 2016, **109**, 053903.
185 L. Shi, C. Ling, Y. Ouyang and J. Wang, *Nanoscale*, 2017, **9**, 533–537.
186 X. Ren, Z. Li, H. Qiao, W. Liang, H. Liu, F. Zhang, X. Qi, Y. Liu, Z. Huang, D. Zhang, J. Li, J. Zhong and H. Zhang, *ACS Appl. Energy Mater.*, 2019, **2**, 4774–4781.
187 S. Shen, Y. Gan, X.-x. Xue, J. Wei, L.-m. Tang, K. Chen and Y. Feng, *Appl. Phys. Express*, 2019, **12**, 075502.
188 Z. Yuan, J. Li, M. Yang, Z. Fang, J. Jian, D. Yu, X. Chen and L. Dai, *J. Am. Chem. Soc.*, 2019, **141**, 4972–4979.
189 Y. Li, J. Chen, J. Huang, Y. Hou, L. Lei, W. Lin, Y. Lian, X. Zhonghua, H.-H. Yang and Z. Wen, *Chem. Commun.*, 2019, **55**, 10884–10887.
190 Y. Singh, S. Back and Y. Jung, *Phys. Chem. Chem. Phys.*, 2018, **20**, 21095–21104.
191 F. Shi, Z. Geng, K. Huang, Q. Liang, Y. Zhang, Y. Sun, J. Cao and S. Feng, *Adv. Sci.*, 2018, **5**, 1800575.
192 L. Zhang, L.-X. Ding, G.-F. Chen, X. Yang and H. Wang, *Angew. Chem., Int. Ed.*, 2019, **58**, 2612–2616.
193 M. Bat-Erdene, G. Xu, M. Batmunkh, A. S. R. Bati, J. J. White, M. J. Nine, D. Losic, Y. Chen, Y. Wang, T. Ma and J. G. Shapter, *J. Mater. Chem. A*, 2020, **8**, 4735–4739.
194 L. Li, C. Tang, B. Xia, H. Jin, Y. Zheng and S.-Z. Qiao, *ACS Catal.*, 2019, **9**, 2902–2908.
195 R. Zhang, L. Ji, W. Kong, H. Wang, R. Zhao, H. Chen, T. Li, B. Li, Y. Luo and X. Sun, *Chem. Commun.*, 2019, **55**, 5263–5266.
196 N. Han, Y. Wang, H. Yang, J. Deng, J. Wu, Y. Li and Y. Li, *Nat. Commun.*, 2018, **9**, 1320.
197 Q. Sun, Z. Li, D. J. Searles, Y. Chen, G. Lu and A. Du, *J. Am. Chem. Soc.*, 2013, **135**, 8246–8253.
198 X. Tan, H. A. Tahini and S. C. Smith, *ACS Appl. Mater. Interfaces*, 2017, **9**(23), 19825–19830.
199 H. Shen, Y. Li and Q. Sun, *Nanoscale*, 2018, **10**, 11064–11071.
200 S. Zhou, W. Pei, J. Zhao and A. Du, *Nanoscale*, 2019, **11**, 7734–7743.
201 B. Luo, G. Liu and L. Wang, *Nanoscale*, 2016, **8**, 6904–6920.
202 A. K. Singh, K. Mathew, H. L. Zhuang and R. G. Hennig, *J. Phys. Chem. Lett.*, 2015, **6**, 1087–1098.
203 J. Yan, P. Verma, Y. Kuwahara, K. Mori and H. Yamashita, *Small Methods*, 2018, **2**, 1800212.
204 A. Maibam, D. Chakraborty, K. Joshi and S. Krishnamurty, *New J. Chem.*, 2021, **45**, 3570–3580.
205 B.-J. Wang, X.-H. Li, R. Zhao, X.-L. Cai, W.-Y. Yu, W.-B. Li, Z.-S. Liu, L.-W. Zhang and S.-H. Ke, *J. Mater. Chem. A*, 2018, **6**, 8923–8929.
206 Y.-L. Lu, S. Dong, W. Zhou, S. Dai, B. Zhou, H. Zhao and P. Wu, *Phys. Chem. Chem. Phys.*, 2018, **20**, 11967–11975.
207 A. Kokabi and S. B. Touski, *Phys. E*, 2020, **124**, 114336.
208 J. Barrio, C. Gibaja, J. Tzadikov, M. Shalom and F. Zamora, *Adv. Sustainable Syst.*, 2019, **3**, 1800138.
209 X.-H. Li, B.-J. Wang, X.-L. Cai, W.-Y. Yu, L.-W. Zhang, G.-D. Wang and S.-H. Ke, *RSC Adv.*, 2017, **7**, 44394–44400.

210 X. Niu, Y. Li, Q. Zhou, H. Shu and J. Wang, *ACS Appl. Mater. Interfaces*, 2017, **9**, 42856–42861.
211 K. Ren, W. Tang, M. Sun, Y. Cai, Y. Cheng and G. Zhang, *Nanoscale*, 2020, **12**, 17281–17289.
212 J. Chu, X. Han, Z. Yu, Y. Du, B. Song and P. Xu, *ACS Appl. Mater. Interfaces*, 2018, **10**, 20404–20411.
213 Y. Gong, J. Shen, Y. Zhu, W. Yan, J. Zhu, L. Hou, D. Xie and C. Li, *Appl. Surf. Sci.*, 2021, **545**, 149012.
214 X. Ji, Y. Kang, T. Fan, Q. Xiong, S. Zhang, W. Tao and H. Zhang, *J. Mater. Chem. A*, 2020, **8**, 323–333.
215 X. Wang, B. Zhou, Y. Zhang, L. Liu, J. Song, R. Hu and J. Qu, *J. Alloys Compd.*, 2018, **769**, 316–324.
216 M. Zhu, M. Fujitsuka, L. Zeng, M. Liu and T. Majima, *Appl. Catal., B*, 2019, **256**, 117864.
217 J. Low, C. Jiang, B. Cheng, S. Wageh, A. A. Al-Ghamdi and J. Yu, *Small Methods*, 2017, **1**, 1700080.
218 J. Hu, D. Chen, Z. Mo, N. Li, Q. Xu, H. Li, J. He, H. Xu and J. Lu, *Angew. Chem., Int. Ed.*, 2019, **58**, 2073–2077.
219 X. Zong, J. Han, G. Ma, H. Yan, G. Wu and C. Li, *J. Phys. Chem. C*, 2011, **115**, 12202–12208.
220 L. Shi, X. Ren, Q. Wang, Y. Li, F. Ichihara, H. Zhang, Y. Izumi, L. Ren, W. Zhou, Y. Yang and J. Ye, *Small*, 2020, **16**, 2002356.
221 B. Qiu, C. Wang, J. Wang, Z. Lin, N. Zhang, L. Cai, X. Tao and Y. Chai, *Mater. Today Energy*, 2021, **21**, 100720.
222 X. Wang, J. He, J. Li, G. Lu, F. Dong, T. Majima and M. Zhu, *Appl. Catal., B*, 2020, **277**, 119230.
223 X. Zhu, S. Huang, Q. Yu, Y. She, J. Yang, G. Zhou, Q. Li, X. She, J. Deng, H. Li and H. Xu, *Appl. Catal., B*, 2020, **269**, 118760.
224 Z.-K. Shen, Y.-J. Yuan, P. Wang, W. Bai, L. Pei, S. Wu, Z.-T. Yu and Z. Zou, *ACS Appl. Mater. Interfaces*, 2020, **12**, 17343–17352.
225 M. Wen, J. Wang, R. Tong, D. Liu, H. Huang, Y. Yu, Z.-K. Zhou, P. K. Chu and X.-F. Yu, *Adv. Sci.*, 2019, **6**, 1801321.
226 J. Lv, M. Xu, S. Lin, X. Shao, X. Zhang, Y. Liu, Y. Wang, Z. Chen and Y. Ma, *Nano Energy*, 2018, **51**, 489–495.
227 W. Hu, L. Lin, C. Yang, J. Dai and J. Yang, *Nano Lett.*, 2016, **16**, 1675–1682.
228 Y. Gao, K. Wu, W. Hu and J. Yang, *Phys. Chem. Chem. Phys.*, 2020, **22**, 28414–28422.
229 C. Zhang, Y. Li, P. Zhang, M. Qiu, X. Jiang and H. Zhang, *Sol. Energy Mater. Sol. Cells*, 2019, **189**, 11–20.
230 F. Zhang, J. He, Y. Xiang, K. Zheng, B. Xue, S. Ye, X. Peng, Y. Hao, J. Lian and P. Zeng, *Adv. Mater.*, 2018, **30**, 1803244.
231 J. M. Tarascon and M. Armand, *Nature*, 2001, **414**, 359–367.
232 H. Shu, F. Li, C. Hu, P. Liang, D. Cao and X. Chen, *Nanoscale*, 2016, **8**, 2918–2926.
233 Q. Tang, Z. Zhou and P. Shen, *J. Am. Chem. Soc.*, 2012, **134**, 16909–16916.
234 H. Hwang, H. Kim and J. Cho, *Nano Lett.*, 2011, **11**, 4826–4830.
235 X.-L. Fan, Y. Yang, P. Xiao and W.-M. Lau, *J. Mater. Chem. A*, 2014, **2**, 20545–20551.
236 Y. Wen, K. He, Y. Zhu, F. Han, Y. Xu, I. Matsuda, Y. Ishii, J. Cumings and C. Wang, *Nat. Commun.*, 2014, **5**, 1–10.
237 Y. Wu, P. Nie, J. Wang, H. Dou and X. Zhang, *ACS Appl. Mater. Interfaces*, 2017, **9**, 39610–39617.
238 L. David, R. Bhandavat and G. Singh, *ACS Nano*, 2014, **8**, 1759–1770.
239 J. M. Soon and K. P. Loh, *Electrochem. Solid-State Lett.*, 2007, **10**, A250.
240 M. Ghidiu, M. R. Lukatskaya, M.-Q. Zhao, Y. Gogotsi and M. W. Barsoum, *Nature*, 2014, **516**, 78–81.
241 L. Shao, H. Sun, L. Miao, X. Chen, M. Han, J. Sun, S. Liu, L. Li, F. Cheng and J. Chen, *J. Mater. Chem. A*, 2018, **6**, 2494–2499.
242 Y. He, Q. He, L. Wang, C. Zhu, P. Golani, A. D. Handoko, X. Yu, C. Gao, M. Ding and X. Wang, *Nat. Mater.*, 2019, **18**, 1098–1104.
243 S. Venkateshwaran and S. M. Senthil Kumar, *ACS Sustainable Chem. Eng.*, 2019, **7**, 2008–2017.
244 Y. Sun, X. Zhang, B. Mao and M. Cao, *Chem. Commun.*, 2016, **52**, 14266–14269.
245 R. Prasannachandran, T. V. Vineesh, A. Anil, B. M. Krishna and M. M. Shaijumon, *ACS Nano*, 2018, **12**, 11511–11519.
246 J. Wu, M. Liu, K. Chatterjee, K. P. Hackenberg, J. Shen, X. Zou, Y. Yan, J. Gu, Y. Yang and J. J. A. M. I. Lou, *Adv. Mater. Interfaces*, 2016, **3**, 1500669.
247 R. Wei, M. Fang, G. Dong, C. Lan, L. Shu, H. Zhang, X. Bu and J. C. Ho, *ACS Appl. Mater. Interfaces*, 2018, **10**, 7079–7086.
248 J. Chen, X. J. Wu, L. Yin, B. Li, X. Hong, Z. Fan, B. Chen, C. Xue and H. Zhang, *Angew. Chem., Int. Ed.*, 2015, **127**, 1226–1230.
249 U. Maitra, U. Gupta, M. De, R. Datta, A. Govindaraj and C. Rao, *Angew. Chem., Int. Ed.*, 2013, **52**, 13057–13061.
250 S. Eyderman and S. John, *Sci. Rep.*, 2016, **6**, 28303.
251 M.-L. Tsai, S.-H. Su, J.-K. Chang, D.-S. Tsai, C.-H. Chen, C.-I. Wu, L.-J. Li, L.-J. Chen and J.-H. He, *ACS Nano*, 2014, **8**, 8317–8322.
252 B. Li, C. Lai, G. Zeng, D. Huang, L. Qin, M. Zhang, M. Cheng, X. Liu, H. Yi, C. Zhou, F. Huang, S. Liu and Y. Fu, *Small*, 2019, **15**, 1804565.
253 Y. Zhang, P. Huang, J. Guo, R. Shi, W. Huang, Z. Shi, L. Wu, F. Zhang, L. Gao, C. Li, X. Zhang, J. Xu and H. Zhang, *Adv. Mater.*, 2020, **32**, 2001082.
254 T. Kaewmaraya, L. Ngamwongwan, P. Moontragoon, W. Jarernboon, D. Singh, R. Ahuja, A. Karton and T. Hussain, *J. Hazard. Mater.*, 2021, **401**, 123340.
255 Y. Liu, Y. Huang and X. Duan, *Nature*, 2019, **567**, 323–333.
256 T. Wu, Y. Ma, Z. Qu, J. Fan, Q. Li, P. Shi, Q. Xu and Y. Min, *ACS Appl. Mater. Interfaces*, 2019, **11**, 5136–5145.
257 Y. Deng, A. D. Handoko, Y. Du, S. Xi and B. S. Yeo, *ACS Catal.*, 2016, **6**, 2473–2481.
258 Y.-F. Huang, P. J. Kooyman and M. T. M. Koper, *Nat. Commun.*, 2016, **7**, 12440.
259 W. Sheng, S. Kattel, S. Yao, B. Yan, Z. Liang, C. J. Hawxhurst, Q. Wu and J. G. Chen, *Energy Environ. Sci.*, 2017, **10**, 1180–1185.
260 Y. Li, Y. Li and Y. Cui, *Chem*, 2018, **4**, 2250–2252.
261 Y. Li, W. Huang, Y. Li, W. Chiu and Y. Cui, *ACS Nano*, 2020, **14**, 9263–9276.

262 Z.-L. Xu, J.-Q. Huang, W. G. Chong, X. Qin, X. Wang, L. Zhou and J.-K. Kim, *Adv. Energy Mater.*, 2017, **7**, 1602078.
263 H. Huang, J. Wang, X. Yang, R. Hu, J. Liu, L. Zhang and M. Zhu, *Angew. Chem., Int. Ed.*, 2020, **132**, 14612–14618.
264 M. Ding, Q. He, G. Wang, H.-C. Cheng, Y. Huang and X. Duan, *Nat. Commun.*, 2015, **6**, 7867.
265 H. Yang, Q. He, Y. Liu, H. Li, H. Zhang and T. Zhai, *Chem. Soc. Rev.*, 2020, **49**, 2916–2936.
266 H. Li, X. Zhou, W. Zhai, S. Lu, J. Liang, Z. He, H. Long, T. Xiong, H. Sun, Q. He, Z. Fan and H. Zhang, *Adv. Energy Mater.*, 2020, **10**, 2002019.
267 Y. Chen, Z. Lai, X. Zhang, Z. Fan, Q. He, C. Tan and H. Zhang, *Nat. Rev. Chem.*, 2020, **4**, 243–256.